PASSIVE DAMPING IN REPULSIVE-FORCE-BASED MAGLEV SYSTEMS

Argonne National Laboratory Report

Prepared For the Federal Railroad Administration

Under Interagency Agreement No. DTFR53-96 X00029

By

Donald M. Rote, Jianliang He*, and Yigang Cai**

***Lucent Technologies Inc.**
****ET Division of ANL**

March, 2001

Center For Transportation Research
Argonne National Laboratory
9700 S. Cass Avenue
Argonne, IL 60439

Dedication

One of the authors, Donald M. Rote, wishes to dedicate this report with love and deep appreciation to his wife, Zenia M. Rote, who has stood by him throughout his career. She has been a companion and understanding helpmate and during the past twelve or so years, has even been an enthusiastic supporter of maglev technology. Following his "retirement" from Argonne in February 2000, she has patiently supported his efforts to complete of this report.

Acknowledgements

This report and the research described herein could not have been undertaken and completed without the support of Dr. John Harding and the funding provided by the Department of Transportation, Federal Railroad Administration. One of the authors, Donald M. Rote, would like to thank the staff of the Center For Transportation Research, Argonne National Laboratory for continuing to provide the necessary facilities, management and secretarial support to complete this work after his formal retirement in February, 2000.

Donald M. Rote wishes to express his gratitude to Anant Vyas for his assistance in solving many vexing computer –related problems that arose during the course of this work. Finally, he wishes to thank Dr. Kent Davey and Dr. Brian Concannon for their reviews of a draft version of this report and also for the many helpful and valued technical discussions they have had about maglev technology.

Abstract

A major objective of this investigation was to reconcile the lack of intrinsic magnetic damping with the absence of observed dynamic instabilities in large-scale repulsive-force based maglev systems. The focus was on the identification and evaluation of various passive damping mechanisms, and whether there were, in fact, sources of enhanced passive damping that compensated for the lack of intrinsic magnetic damping in repulsive force systems

Estimates were first made of the drag force caused by eddy currents induced in guideway electrical conductors, (i.e., non-magnetic rebar, null-flux lift coil conductors, and propulsion coil conductors) during steady-state vehicle motion in the x-direction. Then, damping forces associated with eddy-currents induced in these conductors by unsteady motion (i.e. oscillations in the y or z-directions) were evaluated. The computational method employed readily available formulas for eddy current losses in round conductors and the computation of magnetic fields and there derivatives with a numerical computer model based on the Biot and Savart law. It was found that the drag forces and damping associated with the eddy currents induced in the guideway conductors increased rapidly with conductor radius. In fact the eddy currents induced in the large-radius null-flux coil conductors by motion in the lateral or vertical directions relative to the superconducting magnets was the dominant source of damping. It was also found that by replacing thick coil conductors with stranded cables using individually insulated strands could substantially reduce the drag force. Unfortunately, the use of such cables also substantially reduced the damping force.

The study also examined damping involving the dissipation of eddy currents induced in vehicle-borne, simulated damping plates by vertical and lateral motions relative to the null-flux lift and propulsion coils fixed to the guideway. Dynamic circuit theory was used to model the interaction of the guideway coils and damping plates, which were simulated by single, shorted-turn coils. Two damping coils were used to simulate a damping plate in the case of the null-flux coil induced currents. One damping coil was used in the case of the propulsion coils. It was found that the damping coefficients decreased with vibration frequency and those ascribed to the null-flux/damping coil interaction were generally much larger than those associated with the propulsion coil/damping coil interaction. However, at the null-flux or neutral position, the null-flux-based mechanism produced no lateral damping while the propulsion-coil mechanism did produce some damping, although it was not significant.

When the null-flux coils were designed to minimize the steady-state drag force, the eddy currents induced in the vehicle-borne, simulated damping plates by the null-flux coils became the dominant source of damping in the vertical direction. This mechanism also yielded the largest lateral damping except near the null-flux position, where it went to zero. The damping in the vertical direction decreased with the displacement from the null-flux position while the lateral damping increased. However, even the maximum vertical damping by this mechanism was relatively small, corresponding to a decay time of about 9s.

A further investigation of the null-flux coil/simulated damping plate model indicated that the frequency dependence of the damping force was somewhat sensitive to the choice of equivalent damping coil parameters. The magnitude of the peak damping force in the range of 1 to 10 Hz was less sensitive.

The net effect of all of the passive damping mechanisms examined here appears to be sufficient to overcome the intrinsic negative damping seen in some laboratory experiments and to contribute some net positive damping particularly of large amplitude oscillations in the vertical direction. When the rebar and null-flux lift coils are designed to minimize the steady-state drag forces, the net passive damping is considerably reduced. In particular, the net damping in the lateral direction was found to be very small, suggesting an under-damped condition especially near lift off.

The results of this study were interpreted in light of past findings of laboratory and field tests of maglev systems.

TABLE OF CONTENTS

1. Introduction 11

2. Damping Mechanisms 15

3. Drag Forces and Damping Associated With Eddy Currents Induced In Guideway Conductors 17

   3.1 Steady-State Power Dissipation and Associated Drag Forces 17

   3.2 Damping Forces 27

4. Passive Damping Caused By Eddy Currents Induced In Vehicle-Borne Conductors By Motions Relative To Null-Flux Lift Coils 30

   4.1 Theoretical Model of Passive Damping Due to Eddy Currents Induced in Damping Plates by Motion Relative to the Null-Flux Lift Coils. 33

   4.2 Results of Calculations of Damping Caused by Eddy Currents Induced in Damping Coils by the Null-Flux Coils. 42

5. Passive Damping Due To Eddy Currents Induced In Damping Plates By Motion Relative To The Propulsion Coils 47

   5.1 Theoretical Model of Passive Damping Due to Eddy Currents Induced in Damping Plates by Motion Relative to the Propulsion Coils 48

   5.2 Results of Calculations of Damping Caused by Eddy Currents Induced in Damping Coils by the Propulsion Coils. 50

6. Summary Of Analysis Of Passive Damping Mechanisms 53

7. Damping Associated With Power Pickup **64**

8. Conclusions **65**

References 67

PASSIVE DAMPING IN REPULSIVE-FORCE-BASED MAGLEV SYSTEMS

1. Introduction

In the last several years there has been a renewed interest in the subject of damping of magnetically suspended systems and the related subject of dynamic stability of such systems [1-9]. This renewed interest has focused primarily on repulsive-force, or so-called electrodynamic suspension (EDS) systems, such as the Japanese system currently being tested at the Yamanashi Test Track in Japan. The evidence reported by these investigators strongly supports the often quoted conjecture that while repulsive-force systems are inherently stable, there are circumstances where instabilities can arise. This suggests that the notion of stability in such systems needs careful consideration.

The term "inherently stable" actually has a rather narrow meaning. It refers to the fact that a magnet placed above the surface of a rapidly moving conductor such as the surface of a rotating aluminum cylinder will encounter a repulsive or lift force to counter the force of gravity. Pushing the magnet closer to the surface increases the repulsive force and pulling it away reduces it. A more accurate way to describe this situation is to say that the repulsive-force system is stable under steady-state conditions. This is in contrast to the case of a magnet suspended below a ferromagnetic material by the force of attraction. The latter case is intrinsically unstable and the only way that stable suspension can be achieved is by constantly monitoring the air gap and feeding back this information to a control circuit that continuously adjusts the magnet's excitation in response to changes in the air gap[†]

As already mentioned, in spite of this inherent stability of repulsive-force systems, there is ample theoretical and experimental evidence to show that instabilities can arise under certain circumstances. (See Ref. 2 for a review of the literature on this subject.) These circumstances are generally associated the dynamic response to disturbances of a system that lacks sufficient positive damping or even exhibits negative damping. Systems that lack sufficient damping to rapidly diminish oscillations or prevent the growth of oscillations in response to periodic disturbances are described as under damped. Physically, the disturbances are adding energy to the mode of oscillation faster than the damping mechanism can remove it. Negative damping means that the oscillations in a particular mode due to a disturbance actually grow with time. Negative damping can arise when the disturbed mode of oscillation is coupled to an energy source such as the propulsion motor. Generally, the geometry of an

[†] An exception to this rule was demonstrated at the 6th International Symposium On Superconductivity held on Oct. 26-29, 1993 in Hiroshima, Japan, where staff from the International Superconductivity Technology Center suspended a 10 Kg sphere below a high temperature bulk superconductor cooled to liquid nitrogen temperature. A permanent magnet was fixed to the top of the sphere and its field lines were held within the bulk superconductor by fixed pinning centers.

EDS system couples the vehicle-borne magnets, guideway-mounted lift and guidance coils, and propulsion windings together via the magnetic flux in the magnet air gap. Changes in the length of the air gap between the lift coils, propulsion windings, and on-board magnets caused by a disturbance of the vehicle's position relative to the guideway results in changes in the induced currents in these conductors. Depending on the phase relationships between these changes in induced currents, the disturbed motion may exponentially grow or decay. Several investigators[4,10-15] have shown that when the intrinsic magnetic damping is the only form of damping present, the damping changes from positive to negative near a critical speed defined by

$$V_c = 2/(\mu\sigma\ell_c),$$

where l_c is a characteristic length (for the continuous sheet guideway l_c is taken as the sheet thickness).

In this report, the term "intrinsic magnetic damping" is used to refer to the damping inherently present in an EDS system excluding any enhancements due to added passive damping plates or coils and any active damping mechanisms. The term "negative intrinsic magnetic damping" refers to the situation described above where the intrinsic magnetic damping is negative and the disturbed motion increases with time exponentially.

Fortunately, intrinsic magnetic damping is by no means the dominant form of damping in practical magnetically suspended systems. In fact, the weak or even negative damping characteristics of repulsive-force magnetically-suspended systems can only be observed under conditions where all other forms of damping are either very weak or their effects are carefully subtracted from the total damping. The latter include mechanical or structural and aerodynamic damping, which are often equal to or greater in magnitude than the intrinsic magnetic damping. In addition, large or full-scale systems generally incorporate some form of enhanced passive or active damping to achieve an appropriate level of ride quality. Together, these other forms of damping generally completely mask the intrinsic magnetic damping. Hence, the consequences of the weak or negative intrinsic magnetic damping are difficult to observe in tests of large-scale systems.

For example, tests performed at SRI[16] on a relatively large EDS model showed no evidence of instabilities when subjected to perturbations, although there was some indication of weak damping prior to the incorporation of an active control system. Similarly, tests performed at the Miyazaki Test Track on a full-scale EDS vehicle subjected to large perturbations showed no evidence of instabilities above the lift-off speed[17,18,19]. However, two points are worth noting in regard to these latter tests. First, they did indicate large displacements in response to single and double irregularities deliberately set in the guideway[19]. And, second, as mentioned by the authors[19], the vertical displacement

increased with vehicle speed indicating that a resonant condition was being approached at a somewhat higher speed than had been tested. The maximum test speed was 300 km/h.

Nevertheless, several types of instabilities have been observed in tests of repulsive force magnetically suspended systems[2,5,20,21,22]. These include both static and dynamic instabilities. The former arise, as their name implies, from the static properties of particular magnet/guideway conductor configurations and the variation of the magnetic forces with displacement from an equilibrium position. That is, for certain magnet configurations the force magnitudes or their gradients are insufficient to restore equilibrium following a displacement of sufficient magnitude.

Dynamic instabilities are more complex in nature and are influenced by the geometry of the magnets and guideway conductors, the variation of the forces with velocity and displacement, and the coupling of various modes of motion. The modal coupling arises because the various modes are influenced by changes in the magnetic flux in the magnet air gaps.

A theoretical study at Argonne National Laboratory (ANL)[8] of instabilities of a three-degree of freedom system with a double L-shaped guideway gave examples of flutter instabilities (coupled roll-sway motions) and divergences (initial displacement increases without oscillation).

Tests of a full-scale system at the Yamanashi Test Track reported by Yoshioka et al[5] found that a coupled roll-lateral instability was observed near the lift-off speed, and in fact set a lower limit to a safe lift-off speed. This coupled roll-sway or roll-lateral motion is apparently characteristic of any magnetically suspended repulsive-force system that responds to a lateral displacement by increasing the lateral and vertical forces on one side relative to the other. (Of course, the existence of this modal coupling does not necessarily imply an instability.) Examples of maglev designs that decouple the roll and sway motions are described in Ref. 23 and 24. However, these designs do couple heave (vertical) and sway (lateral) motion. This latter coupling provides a relatively large resistance to lateral motions because any lateral motion must also lift the vehicle instead of just rolling it about a longitudinal axis.

Kolm[22] has reported that early experiments at MIT employing a rectangular cross-section, continuous-sheet guideway showed large-amplitude yaw oscillations that resulted in contact of the model vehicle with the guideway and even resulted in derailment in some cases. He referred to the observed phenomenon as a “drag-force induced instability”, which was caused by the increase in drag force when the lateral air gap between vehicle borne magnets and aluminum sidewall is reduced due to a lateral disturbance. Kolm noted that the increased drag force on one side or one corner of the vehicle creates a yaw torque which is subsequently counteracted by the torque exerted by the guidance forces.

This in turn results in a yaw oscillation that if not sufficiently damped will grow exponentially until the guideway wall is contacted.

Curiously, the "drag-force induced instability" was not observed in the SRI or the Miyazaki tests as noted above, although it was observed in small-scale laboratory experiments at ANL[2], Cornell University[20,21], MIT [22], and elsewhere (see Ref. 2 for a review). This suggests that there were factors present in the SRI and Miyazaki tests that served to suppress the instability. Since no detailed study has ever been done comparing these various tests, it is difficult to say with certainty what those factors were. However, some points are clear: First, the ANL and Cornell experiments included only intrinsic magnetic damping and presumably the MIT experiments had very little if any damping other than the intrinsic magnetic damping since the cryostat walls were very thin. On the other hand, both the SRI and Miyazaki tests had significant amounts of enhanced passive damping. The SRI superconducting magnets[25] (SCM's) included large cross-section, shorted, single-turn damping coils cooled with liquid nitrogen, which provide significant damping forces. The Miyazaki SCM's[26] incorporated thick outer cryostat walls which act as damping plates. Second, the magnet/guideway conductor configuration differences may have also been important. The SRI guideway consisted of two thick L-shaped continuous sheets with low sidewalls, whereas the Miyazaki guideway consisted of shorted-turn coils mounted on the ground and sidewall-mounted propulsion coils cross connected to provide null-flux guidance. The ANL guideway consisted of two L-shaped rims mounted on a rotating wheel. The Cornell experiments used both continuous sheet double L's and discrete double L's mounted on rotating wheels. The MIT experiments used linear tracks with round and rectangular cross sections. In addition, the Miyazaki vehicles used null-flux guidance, whereas the other systems used direct magnet/induced eddy current interactions to produce the guidance forces. Null-flux configurations have been shown to produce substantially stiffer forces than the latter[27]. This means that, in the Miyazaki case, the gradients of the guidance forces and the associated restoring torques may have been substantially greater than the drag force gradients and torques. This latter factor would make the Miyazaki vehicle very resistant to yaw motion.

Based upon these points,, it is proposed that three conditions should be present to suppress the drag-force induced instability. First, the guidance forces must be sufficiently stiff to limit yaw and lateral motion, and the length to width ratio of the vehicle must be large enough so that the associated guidance torque will greatly exceed the drag-force induced yaw torque. Second, the vehicle structure must be sufficiently stiff to transmit the torques without inducing large internal vibrations. And third, there must be sufficient enhanced lateral damping to prevent exponential growth at any resonant frequency.

Finally, it is now well established that intrinsic magnetic damping is generally weak and, depending on the magnet/guideway conductor configuration, may change from positive to small negative values as the speed is increased through a characteristic value. With further increases in speed the intrinsic damping reaches a minimum value then approaches zero or some small positive value again. Yet, there is no evidence reported from any of the tests conducted on full-scale vehicles at Miyazaki or Yamanashi of a lack of damping or an instability in the high-speed regime (i.e. well above the lift-off speed). Consequently, there must be one or more sources of damping that shall be referred to as enhanced passive damping mechanisms that are more than adequate to maintain dynamic stability at high speeds. This being the case, what are those enhanced passive damping mechanisms? This is the subject of the remainder of this report.

2. Damping Mechanisms

Damping mechanisms of interest here are those mechanisms that damp out the unwanted motion of a magnetically suspended vehicle caused by a disturbance or perturbing force. In general, the unwanted motion can be described as the excitation of one or more modes of vibration of the system. These modes are often coupled together by the air gap flux. Thus, even though the original disturbance may be attributed to a displacement acting in only one mode, the coupling can subsequently transfer energy to other modes as well. Similarly, damping of one of the excited modes may result in damping of other modes.

In general the disturbing force may be transitory, such as a wind gust or an irregularity in the guideway, or periodic in nature such as may result from a flexible guideway that is supported by pillars at regular intervals. Damping mechanisms work by removing energy from the unwanted motions in one or more of the coupled modes excited by the disturbing force. The removed energy may be dissipated as waste heat or transformed into some useful form. If the damping is negative, it can cause some energy to be transferred from another energy source such as the propulsion motor into the originally disturbed mode, increasing the extent of the disturbance.

In this report, a distinction is made between electromagnetic drag forces and damping forces. Drag forces are present regardless of whether or not there are disturbances. They can arise from several sources including I^2R losses due to the electromotive forces induced in the guideway lift and guidance coils, eddy currents induced in thick windings of those coils and in metallic fasteners and guideway structural members including re-enforcing rods (rebar). They can also result from the transfer of energy from electromagnetic coupling between on-board linear generator coils and guideway coils. Since all of these sources of drag force are dependent on the magnetic flux in the air gaps, fluctuations in those air gaps caused by perturbations (vehicle or guideway displacements) will affect the

magnitudes of the drag force terms to some extent. Even though the effects of these fluctuations may be relatively small compared to the steady-state drag forces, they are also sources of damping of vehicle oscillations.

In contrast to the steady-state drag forces , damping forces only arise in response to disturbances. The various damping mechanisms can be roughly classified according to whether the primary energy dissipation mechanism is electromagnetic, mechanical, or aerodynamic in nature. Generally, in a practical system, all three of these types of damping mechanisms operate jointly. The mechanisms may be further classified according to whether they are active (i.e. involving the use of control systems incorporating feedback) or passive, and if passive, whether they are naturally occurring (e.g., intrinsic magnetic damping), or enhanced in some way. In the present paper, attention will be focused primarily on passive electromagnetic damping mechanisms. Such mechanisms generally involve the induction of electromotive forces in conductors that are put in motion relative to magnetic field sources by some disturbance. Such mechanisms include the following:

1) Ohmic heating due to eddy currents induced in metallic guideway components such as rebar and fasteners by fluctuations in the relative lateral or vertical positions of vehicle-borne superconducting magnets (SCM's).
2) Ohmic heating due to eddy currents induced in the guideway-mounted coil windings by fluctuations in the relative lateral or vertical positions of vehicle-borne SCM's.
3) Ohmic heating due to eddy currents induced in vehicle-borne damping plates or metallic cryostat walls by motion relative to null-flux lift coils.
4) Ohmic heating due to eddy currents induced in vehicle-borne damping plates or metallic cryostat walls by motion relative to the propulsion coils.
5) A damping mechanism that does not necessarily involve ohmic heating is the transfer of energy from the guideway to the vehicle through inductive pickup coils. Fluctuations in the air gap between the pick up coils and the field sources will lead to changes in the amount of energy transferred and hence result in a form of damping

Mechanisms 1 and 2 are discussed and evaluated in Sec. 3. The third and fourth mechanisms are treated in detail in Sec's. 4 and 5, respectively. The results of evaluating the various passive damping mechanisms are summarized in Sec. 6. The fifth damping mechanism is addressed briefly in Sec. 7. Damping mechanisms incorporated into secondary suspension systems, i.e., those that suppress motion between the primary magnetic suspension system and the car body, are not treated in this report.

3. Drag Forces and Damping Associated With Eddy Currents Induced in Guideway Conductors

Under steady-state conditions the movement of a vehicle along the guideway exposes the metallic guideway components to time-varying magnetic fields. This exposure induces currents to flow in the lift, guidance and propulsion coils that, in turn, result in the forces that govern the vehicle's position and motion. In addition to producing those forces, the induced currents also result in I^2R losses that heat the coils and cause electromagnetic drag forces. Also during steady-state motion, eddy currents are induced in the rebar and the coil conductors that contribute to the losses and drag forces.

Under perturbed motions, the guideway components are also exposed to additional magnetic field variations which are superimposed on the steady-state variations and, in turn, induce eddy currents which are dissipated by ohmic heating. The power dissipated by the latter eddy currents under the perturbed motions results in a damping of the perturbations. Consequently these guideway components provide a source of damping as well as steady-state drag forces.

The steady-state power dissipation and associated drag forces caused by induced eddy currents are discussed first, followed by the damping forces that act in the presence of perturbed motions.

3.1 Steady-State Power Dissipation and Associated Drag Forces.

Formulas for the average power dissipated in round conductors or sheet laminations exposed to alternating magnetic fields can be found in Ref. 28. For round conductors of radius r and conductivity σ, the average power dissipated per unit volume of conductor is given in MKS units by:

$$P_e\,(\mathrm{W/m^3}) = 0.25[\pi.r(\mathrm{m}).f(\mathrm{Hz}).B_0(\mathrm{T})]^2\sigma(\mathrm{S/m}), \qquad (1)$$

where f and B_0 are the frequency and amplitude, respectively, of the sinusoidal-varying magnetic field caused by a series of vehicle-borne, alternating polarity magnets sweeping past the guideway.

In addition, Zahn and his students at MIT[29] carried out calculations of power loss in both magnetic and non-magnetic materials used for rebar. As noted in Refs. 29 and 30, ordinary steel rebar is magnetic and not suitable for use near the magnets used in EDS maglev systems. Hence, only non-magnetic steel rebar will be considered here. According to Ref. 29, in the large skin depth limit, the dissipated power is given as follows:

In the axial case, i.e., the rod is oriented parallel to **B**,

$$\langle P \rangle_{axial}(W/m) = 0.25\pi r^4 B_0^2 \sigma \left(\pi f \frac{\mu}{\mu_0} \right)^2 . \tag{2a}$$

In the transverse case, i.e., when the rod is oriented perpendicular to **B**,

$$\langle P \rangle_{trans}(W/m) = 0.5\pi r^4 B_0^2 \sigma \left(\pi f \frac{\mu}{\mu_0} \right)^2 \left(\frac{2\mu_0}{\mu + \mu_0} \right)^2 . \tag{2b}$$

It should be noted that, in the case where $\mu \approx \mu_0$, and Eqn. (2a) is expressed in terms of the average power per unit volume of a rod instead of per unit length, it is identical to Eqn. 1. In addition, when $\mu \approx \mu_0$, Eqn. (2b) is seen to be twice as large as Eqn. (2a) for the same values of r, B_0, σ, and f.

An estimate of the relative contributions to the dissipated power per unit length and the associated drag force† from various materials used in the guideway can be obtained by examining the corresponding values of the parameters r, B_0, σ. In the large skin depth limit (f < 2000 Hz for non-magnetic materials), the dissipated power per unit length will depend on the product of the rod-radius to the fourth power, the maximum magnetic flux density squared, and the conductivity. The steady state drag force associated with this power dissipation is obtained by dividing either Eqn. (2a) or (2b) by the velocity. Table 1 (Ref. 29) gives the properties of two materials of interest. Based on these data, aluminum conductors, on a per unit length basis, are at least an order of magnitude more important than rebar in terms of power dissipated and the associated drag force.

Table 1 Properties of Guideway Materials

Material	Permeability (4π e-7)	Conductivity (S/m)	Typical Radius (m)	$\approx B_0$ (T)	Product ($\sigma B^2 r^4$)
Aluminum	1	3.53 e 7	0.00423 to 0.00733	0.83	0.0078 to 0.070
13% Mn Steel	1.01	1.41 e 6	0.00635 to 0.0127	0.06 to 0.6	8.3 e-6 to 0.013

† The drag force addressed here is that associated with the dissipation of power due to eddy currents induced in rebar and guideway-mounted lift coils. It is not the same as the drag force caused by the currents induced in the lift coils that produces the lift force. The latter drag force reaches a peak value at a relatively low speed and decreases as the speed increases. The eddy-current drag force being addressed here increases with speed (frequency).

To obtain a better estimate of the contributions of aluminum conductors and rebar, it is necessary to take into account a number of details that considerably complicate the problem. To simplify the problem, the following assumptions will be made:

The field source consists of superconducting magnets (SCM's) placed at the ends of each maglev vehicle. There are four superconducting coils per SCM as shown in Fig. 1b. All are in the same x-z plane at y = 0. (See Fig. 1a for the coordinate system used in this report).

There are three aluminum lift coils per superconducting coil in the guideway (See Fig. 1c). These coils are all in the x-z plane at y = - 0.185 m.

The guideway is assumed to be u-shaped with non-magnetic ($\mu \approx \mu_0$) rebar aligned in the x- and z-directions in the sidewalls and in the x- and y- directions in the guideway base or floor. Crossing rebar are assumed to make no electrical contact. Note that if the crossing rebar did make electrical contact then currents would also be induced in the resulting closed circuit loops , which would lead to additional losses.

The rebar in the sidewall are all located in the x-z plane at y = 0.4 m.

The rebar in the floor are all in the x-y plane at z = - 0.475 m.

The variations in the magnetic field seen by the rebar and coil conductors are sinusoidal.

Generally, as a series of magnets sweep past a piece of rebar, the rebar will see a combination of periodic transverse and axial field components. Provided that these periodic field components are sinusoidal, Eqns (2a) and (2b) apply, and can be combined to give

$$\langle P \rangle = 0.5\pi^3 \sigma f^2 r^4 \left[B_T^2 + 0.5 B_A^2 \right], \tag{2c}$$

where B_T and B_A are the amplitudes of the transverse and axial fields, respectively. In terms of the components of the magnetic field in Cartesian coordinates, B_T and B_A are:

$B_T^2 = B_x^2 + B_y^2$ *and* $B_A^2 = B_z^2$ for the vertical rebar in the sidewalls,

$B_T^2 = B_y^2 + B_z^2$ *and* $B_A^2 = B_x^2$ for the longitudinal rebar in the sidewalls and floor, and

$B_T^2 = B_x^2 + B_z^2$ *and* $B_A^2 = B_y^2$ for the lateral rebar in the floor.

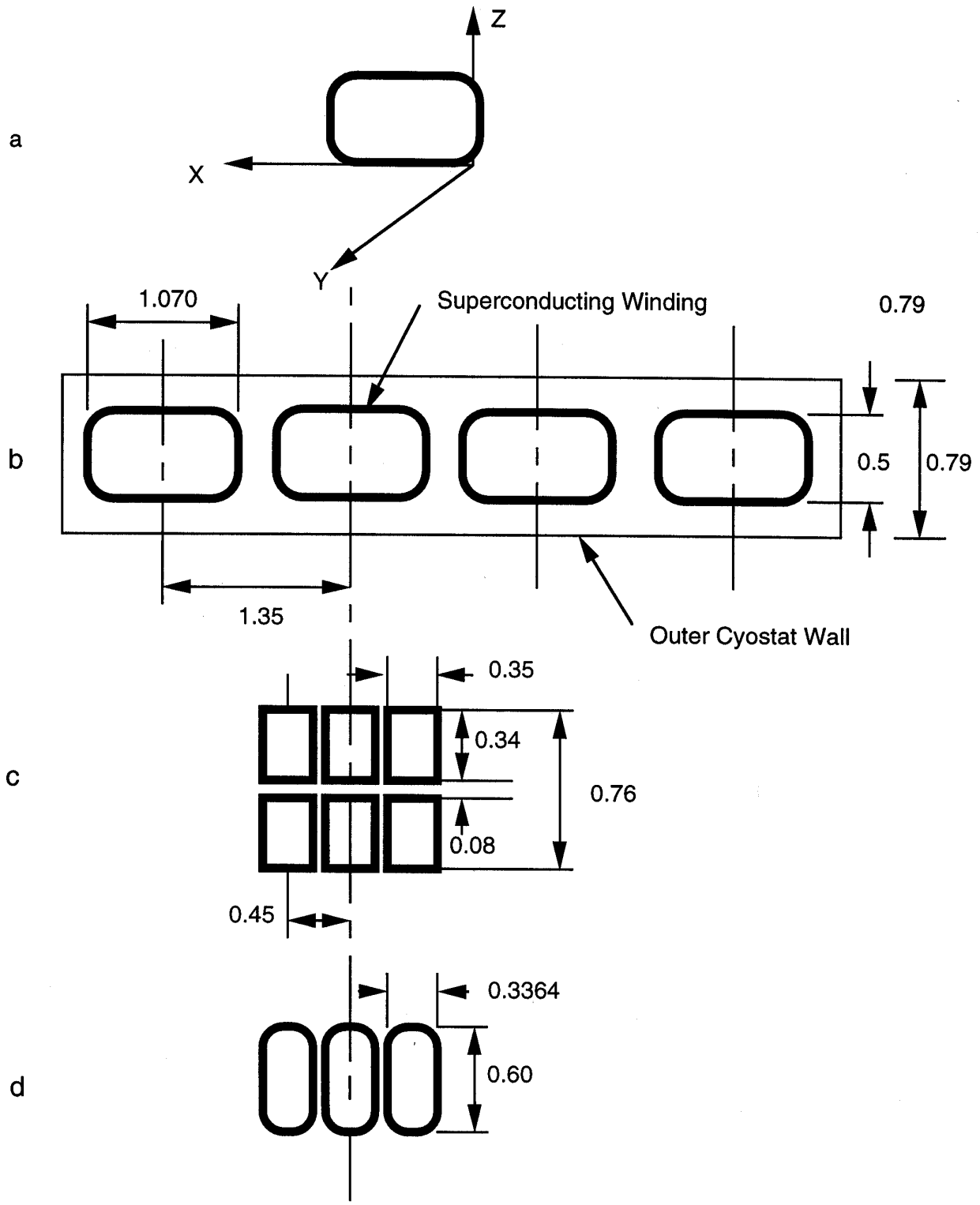

Figure 1. a) Coordinate System; b) Superconducting Magnet With Four Coils; c) Three Null-Flux Lift Coils Facing Each Magnet Coil; d) Three Propulsion Coils Facing Each Magnet Coil.

As the above equations indicate, the axial magnetic fields always consist of one component, whereas the transverse magnetic fields consist of two orthogonal components. Depending on the particular orientation of the rebar and field components, the field components constituting the transverse field may be in phase, 180 degrees out of phase, or 90 degrees out of phase. The first two cases lead to fields oscillating in one transverse direction, while the last case results in a rotating transverse field. In either case the resulting currents are axial in nature and it is assumed that the net power dissipation is approximately the same. The validity of this latter assumption requires further analysis, but will not be addressed here.

For computational convenience, the above expressions for the transverse and axial fields can be combined with Eqn. (2c) to yield:

$$\langle P \rangle = 0.5\pi^3 \sigma f^2 r^4 B^2, \tag{3a}$$

where, for the vertical rebar in the sidewalls,

$$B^2 = B_2^2 = B_x^2 + B_y^2 + 0.5 B_z^2, \tag{3b}$$

for the longitudinal rebar in the sidewalls and floor,

$$B^2 = B_3^2 = B_y^2 + B_z^2 + 0.5 B_x^2, \tag{3c}$$

and, for the lateral rebar in the floor,

$$\mathrm{B}^2 = B_1^2 = B_x^2 + B_z^2 + 0.5 B_y^2. \tag{3d}$$

The Bx, By, and Bz components of the field due to a sequence of four coils constituting a single SCM have been calculated using a numerical procedure based on the law of Biot and Savart, which for a straight line segment carrying current I can be written in the form* :

$$B = \mu_0 I(\sin\theta_r - \sin\theta_l)/4\pi R, \tag{4}$$

where R is the perpendicular distance from the field point to the line segment (or its extension), and θ_r and θ_l are the angles from the field point to the right and left ends of the line segment.

* See http://www.physics.ubc.ca/~beder/MAG-1/sld026.htm

Figure 2a. Bx, By, & Bz Due To 4 Coils Each 0.5 x 1.07, Pitch =1.35, Y= - 0.185, Z= 0.25 (in plane of lift coils)

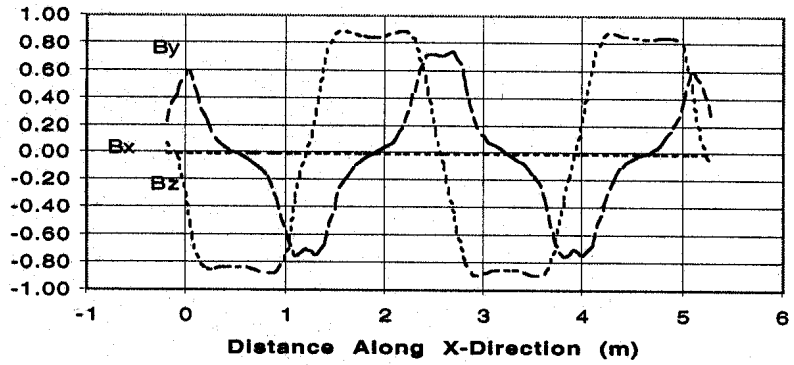

Figure 2b. Same As 2a, With Y= - 0.4, Z= 0.25 (in plane of sidewall rebar)

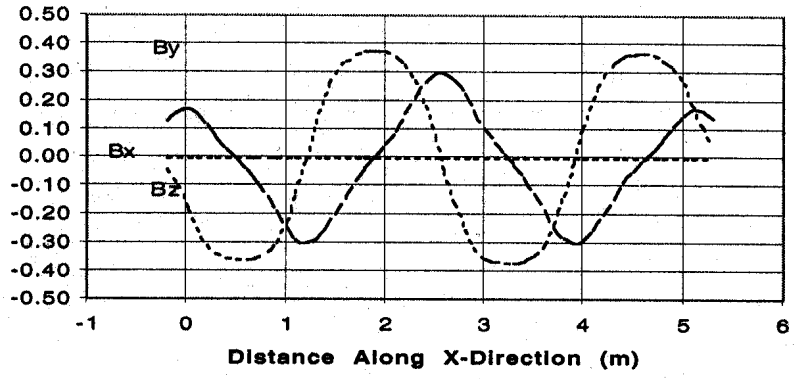

Figure 2c. Same As 2a, With Y= 0, Z= -0.475 (in floor in SCM coil plane)

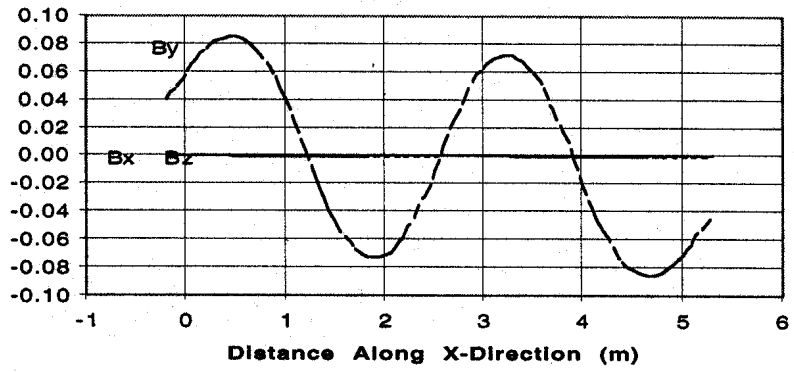

Figure 2d. Same As 2a, With Y= 0.8, Z = -0.475 (In floor 0.8 m from SCM coil plane)

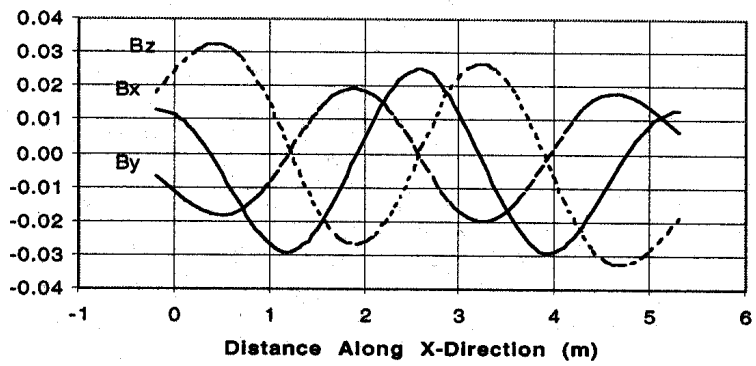

Figure 2e. Square Of B1, B2, & B3 In The X-Z Plane At Y=-0.4

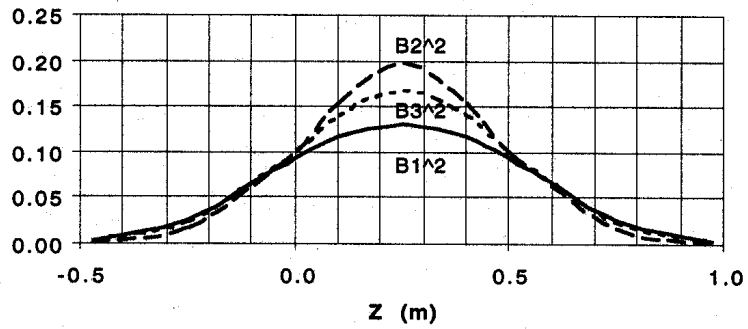

Figure 2f. Square of B1, B2, & B3 In The X-Y Plane At Z = -0.475

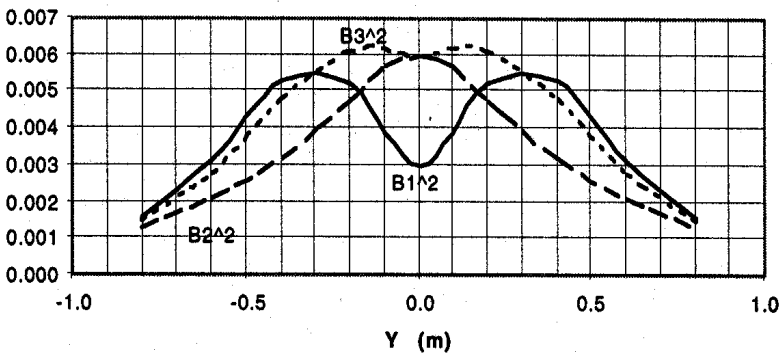

Results of these calculations are illustrated in the series of graphs shown in Fig. 2a – 2d. Fig. 2a shows the field components as a function of x in the x-z plane of the lift coils (y = - 0.185) at the height z = 0.25. Fig. 2b shows a similar plot in the x-z plane of the sidewall rebar (y = - 0.4). As the distance from the SCM plane increases, the curves look more sinusoidal. Fig. 2c shows the field components at the intersection of the SCM and the floor rebar plane. Fig.2d shows the field components in the floor rebar plane 0.8 m from the SCM plane. The parameter values used in the field calculations illustrated in Fig. 2 and in the following power dissipation and drag force calculations are listed in Table 2.

It is evident from the graphs in Fig. 2a-d that the dependence of these field components on x departs from sinusoidal in two respects. First, since there are only four superconducting coils in sequence the variations are aperiodic. Second, because of the rectangular coil geometry, even an infinite sequence of such coils would not produce purely sinusoidal waveforms. Nevertheless, it will be assumed here that the waveforms are sinusoidal and that average amplitudes can be assigned to each component. Essentially, what is being assumed here is that each set of four coils constituting a single SCM interacts with the very long sequence of pieces of guideway rebar (or lift coils) as though there were an infinite sequence of SCM's as well. Physically, this is not an unreasonable assumption because the presence of additional SCM's would not have a large effect on the power dissipation and drag force calculations. However, additional SCM's would directly affect the energy transferred to the guideway metallic components and their resultant temperature rise.

For convenience, the computation of power dissipation and drag force will be made on a per SCM basis. That is, all of the rebar or coils within a length L_S (the length of an SCM) will be considered as a unit. The average power dissipated in rebar per SCM is given by

$$\langle P\rangle(W/SCM) = \langle P\rangle_{TVSW} + \langle P\rangle_{TLSW} + \langle P\rangle_{TCF} + \langle P\rangle_{TLF} \tag{5a}$$

where

$$\langle P\rangle_{TVSW} = C \times N_{VSW} \sum_i \delta z_i B_2^2(y = -0.4, z_i)$$

$$\langle P\rangle_{TLSW} = C \times L_S \sum_j B_3^2(y = -0.4, z_j)$$

$$\langle P\rangle_{TCF} = C \times N_{CF} \sum_i \delta y_i B_1^2(y_i, z = -0.475)$$

$$\langle P\rangle_{TLF} = C \times L_S \sum_j B_3^2(y_j, z = -0.475), \quad \text{where } C = 0.5\pi^3 \sigma r^4 f^2 \tag{5b}$$

and where the sums over the index i are over short segments δz_i of one vertical sidewall rebar and over short segments δy_i of one cross floor rebar, and the sums over the index j add up the contributions from each longitudinal rebar in the sidewall and floor. N_{VSW} is the number of vertical rebar in the sidewall per SCM and N_{CF} is the number of cross rods in the floor per SCM. The average values of magnetic field amplitudes needed in Eqn. (5) are shown in Fig. 2e & 2f, for the sidewall and floor rebar, respectively.

Similarly, the power dissipated by eddy currents induced in the null-flux lift coil vertical and longitudinal conductors and in the propulsion coil vertical and longitudinal conductors are given by

$$\langle P\rangle_{VNF} = 2CN_t N_\ell \sum_i \delta z_i B_2^2\left(y=-0.185, z_i\right) \text{ and}$$
$$\langle P\rangle_{LNF} = CL_{NFC} N_\ell N_t \sum_j B_3^2\left(y=-0.185, z_i\right) \tag{5c}$$

for the null-flux coils and

$$\langle P\rangle_{VP} = 2CN_t N_c \sum_i \delta z_i B_2^2\left(y=-0.24, z_i\right) \text{ and}$$
$$\langle P\rangle_{LP} = CL_{PC} N_C N_t \sum_j B_3^2\left(y=-0.24, z_j\right) \tag{5d}$$

for the propulsion coils, where N_t is the number of turns per coil, N_c is the number of coils per SCM, N_l is the number of null-flux loops per SCM (namely, 24), and L_{NFC} and L_{PC} are the lengths of the null-flux and propulsion coils, respectively*.

* It should be noted that the power dissipation being calculated here is distinct from the I^2R losses associated with currents circulating through the coils that provide the lift, guidance and propulsion forces.

Table 2 Parameters of a Hypothetical EDS Maglev System With a Null-Flux Coil Suspension System.

	Case 1	Case 2	Case 3
No. of SCM's per bogie	2	2	2
SCM pitch (m)	1.35	1.35	1.35
Null-flux coil pitch (m)	0.45	0.45	0.45
Null-flux coil length (m)	0.35	0.35	0.35
Null-flux coil loop height (m)	0.34	0.34	0.34
No, of turns per coil	**48**	**16**	**48**
No. of insulated strands/conductor	-	-	**7**
Null-flux coil conductor radius (mm)	**4.23**	**7.33**	**1.56**
No. of null-flux coils per SCM	12	12	12
Distance from SCM to Null-flux coil plane	0.185	0.185	0.185
Propulsion coil length	0.3364	0.3364	0.3364
Propulsion coil height	0.6	0.6	0.6
No. of coils per SCM	12	12	12
No. of turns per coil	16	16	16
No. of insulated strands/conductor	-	-	**7**
Propulsion coil conductor radius (mm)	**4.308**	**5.45**	**1.56**
Distance from SCM to propulsion coil plane	0.24	0.24	0.24
Rebar material	13%Mn steel	13%Mn steel	
Rebar radius (m)	**0.00794**	**0.01588**	
Rebar spacing	0.1524	0.1524	
Length of vertical rebar (m)	1.4	1.4	
Exposed length of cross floor rebar (m)	1.75	1.75	
No. of vert. rebar in sidewall/SCM	**108**	**27**	
No. of long. rebar in sidewall/SCM	**30**	**8**	
No. of cross rebar in floor/SCM	**108**	**27**	
No. of long. rebar in floor/SCM	**35**	**8**	

Using the data in Tables 1 and 2, and Eqns. (4) and (5), the results are given in Table 3.

Table 3 Eddy Current Losses in Guideway Components Per SCM at 550 (km/h) (152.8 m/s)

	13%Mn Steel Rebar		Null-Flux Lift Coils		Propulsion Coils	
	Power Lost (kW)	Drag Force (kN)	Power Lost (kW)	Drag Force (kN)	Power Lost (kW)	Drag Force (kN)
Case 1	6.8	0.044	589	3.85	83	0.54
Case 2	27.2	0.178	1770	11.6	213	1.39
Case 3			76	0.50	10	0.065

Hence, in terms of the power dissipated and the associated drag force, the null-flux coils are the most important followed by the propulsion coils and the rebar. However, it should be realized that these results are very sensitive to the radii of the rebar and the coil conductors and obviously, the smaller these radii are the better. For the combined best cases, the total dissipated power is 93 kW, whereas for the combined worst cases it is 2.01 MW. For a train consisting of 14 cars (30 SCM's), the total loss ranges from 2.8 to 61 MW. Obviously, considerable care is required to minimize these sources of steady-state power loss and drag force.

3.2 Damping Forces

In the previous section, power dissipation and drag force due to eddy currents induced in various guideway conductors by steady-state motion of the vehicle in the x-direction was estimated. In this section, an estimate is made of the damping force associated with the eddy current losses in rebar and coil conductors in response to unsteady or disturbed vehicle motion in the y- and z-directions. Since these forces are expected to be quite small, a simple approach, based on the equations given in the previous section, may be used to make some rough estimates.

It is assumed that a disturbance in the motion of the vehicle in the y or z-direction is superimposed on the steady-state motion in the x-direction. This disturbance gives rise to oscillatory motion of amplitude $\Delta\xi$ and frequency f and a corresponding oscillation in the amplitude of flux density δB at the site of a conductor in the guideway. Using Eqn. (3) for the large skin depth limit, and assuming only non-magnetic materials, the corresponding power dissipated per unit length of conductor is given by

$$\delta\langle P\rangle_T = 0.5\,\pi^3 r^4 \sigma f^2 \delta B^2 = 0.5\pi^3 r^4 \sigma f^2 \left(\frac{\partial B}{\partial \xi}\right)^2 \Delta\xi^2 \tag{6}$$

where $\Delta\xi$ can be taken as a small displacement in the y or z –direction. If the response to the disturbance is harmonic, then the corresponding average value of the velocity is given by

$$v = 4 f \Delta\xi$$

and the estimated average value of the damping force per unit length of guideway conductor is given by the power dissipated divided by the average value of the velocity in the direction of the disturbance:

$$F_d\left(\frac{N}{m}\right) = \delta\langle P\rangle_T \Big/ v = K\left(\frac{\partial B}{\partial \xi}\right)^2 , \tag{7}$$

where

$$K = 0.125\pi^3 r^4 \sigma f \Delta\xi,$$

and

$$\left(\partial B \big/ \partial\xi\right)^2 = \left(\partial B_x \big/ \partial\xi\right)^2 + \left(\partial B_y \big/ \partial\xi\right)^2 + \left(\partial B_z \big/ \partial\xi\right)^2$$

Expressions similar to those in Eqn. (5) can be written down for the dissipated power in the rebar, null-flux, and propulsion coil conductors due to the disturbed or oscillatory motion of the vehicle. Combining such expressions with Eqn (7) results in the following equations for the damping force contributions from the vertical and longitudinal rebar in the sidewall:

$$F_d = 0.5K \times N_{vsw} \sum_i \delta z_i \left(\partial B \big/ \partial\xi\right)_i^2 \tag{8a}$$

and

$$F_d = K \times L_S \sum_j \left(\partial B \big/ \partial\xi\right)_j^2 \quad ; \tag{8b}$$

For the cross-rebar and longitudinal rebar in the floor:

$$F_d = K \times N_{CF} \sum_i \delta y_i \left(\partial B \big/ \partial\xi\right)_i^2 \tag{8c}$$

and

$$F_d = K \times L_S \sum_j \left(\partial B / \partial \xi \right)_j^2 \quad ; \tag{8d}$$

For the vertical and longitudinal conductors in the null-flux loops:

$$F_d = K \times N_T \times N_L \sum_i \delta z_i \left(\partial B / \partial \xi \right)_i^2 \tag{8e}$$

and

$$F_d = K \times N_T \times N_{NFC} \sum_j \left(\partial B / \partial \xi \right)_j^2 \quad ; \tag{8f}$$

For the vertical and longitudinal conductors in the propulsion coils:

$$F_d = K \times N_T \times N_C \sum_i \delta z_i \left(\partial B / \partial \xi \right)_i^2 \tag{8g}$$

and

$$F_d = K \times N_T \times N_C \times L_{PC} \sum_j \left(\partial B / \partial \xi \right)_j^2 . \tag{8h}$$

Now, to evaluate the above expressions, it is necessary to make some reasonable assumptions about the angular frequency (ω) and amplitude ($\Delta\xi$) of the disturbed motion, and the derivative of the magnetic flux density B with respect to the y or z-direction. Assuming that the disturbed motion occurs at or near some resonant frequency of the suspension system, ω is of the order 30 radians/s (f = 4.77 Hz). The derivative of the B field with respect to y or z at the location of the guideway conductors can be obtained from the calculations of the B field described earlier.

The results of the damping force calculations at 4.77 Hz (30 rad/s) are given in Table 4 as a function of the amplitude of the oscillation ($\Delta\xi$) in the z- or y-direction. The parameter values for cases 1, 2, & 3 are as shown in Table 2. The dominant damping force comes from the eddy currents induced in the null-flux coil conductors due to the number of conductors and their proximity to the SCM's.. In this approximation, the damping force increases linearly with the oscillation amplitude and frequency.

The relative importance of these damping forces will be addressed later. It is worthwhile noting here that when the rebar and coil conductors are designed to reduce the drag forces as much as possible, the corresponding damping forces, which could be considered a side effect, are also reduced proportionately. While the main objective is desirable, the side effect may not be. The more that the drag forces are reduced, the more that the attendant loss of damping must be compensated for by other damping mechanisms.

Table 4 Approximate Damping Forces Per SCM Associated With Eddy Current Losses in Guideway Components Caused By Vehicle Oscillations in the Z- or Y-Direction at 30 (Rad./s).

	Displacement (=δz) (m)	13%Mn Steel Rebar (N/SCM)	Null-Flux Coils (N/SCM)		Propulsion Coils (N/SCM)
Direction of Oscillation			Z	Y	Z
Case 1	0.005	0.09	13.5	24.3	2.0
	0.01	0.182	26.9	48.5	4.0
Case 2	0.005	0.38	40.5	73	5.1
	0.01	0.76	80.9	146	10.2
Case 3	0.005		1.7	3.1	0.24
	0.01		3.5	6.3	0.48

4. Passive Damping Caused by Eddy Currents Induced in Vehicle-Borne Conductors by Motions Relative to Null-Flux Lift Coils

We now shift our attention from passive damping mechanisms involving the induction of eddy currents in guideway components to those involving the induction of eddy currents in vehicle-borne conductors. Conductors that are rigidly fixed to the vehicle and move relative to field sources located on the guideway can contribute to the passive damping of vehicle motions. Such conductors include closed-loop coils deliberately intended to serve as dampers, metallic plates that were intended to serve as eddy-current and thermal shields of superconducting magnets (SCM's) and power pickup coils. These coils and plates are exposed to the superposition of the constant primary fields from the vehicle SCM's, and time-varying fields due to the currents in the guideway coils, which are in motion relative to the vehicle. The time-varying part of the fields consist of a periodic variation associated with the longitudinal steady-state motion of the vehicle along the guideway and other field components associated with non-steady-state vehicle motions in the x, y, and z directions that are caused by perturbing forces. The former contributes to the drag force on the vehicle while the latter contributes to the damping of oscillatory motions in the x, y, and z directions.

Here we will focus attention on the damping effects of shorted, single-turn coils or metallic plates including cryostat walls that can be reasonably well simulated by shorted, single-turn coils.

As illustrated in Fig. 3, cryogenic-liquid-cooled superconducting magnets generally consist of a superconducting winding surrounded by several containment vessels. The inner vessel, which contains

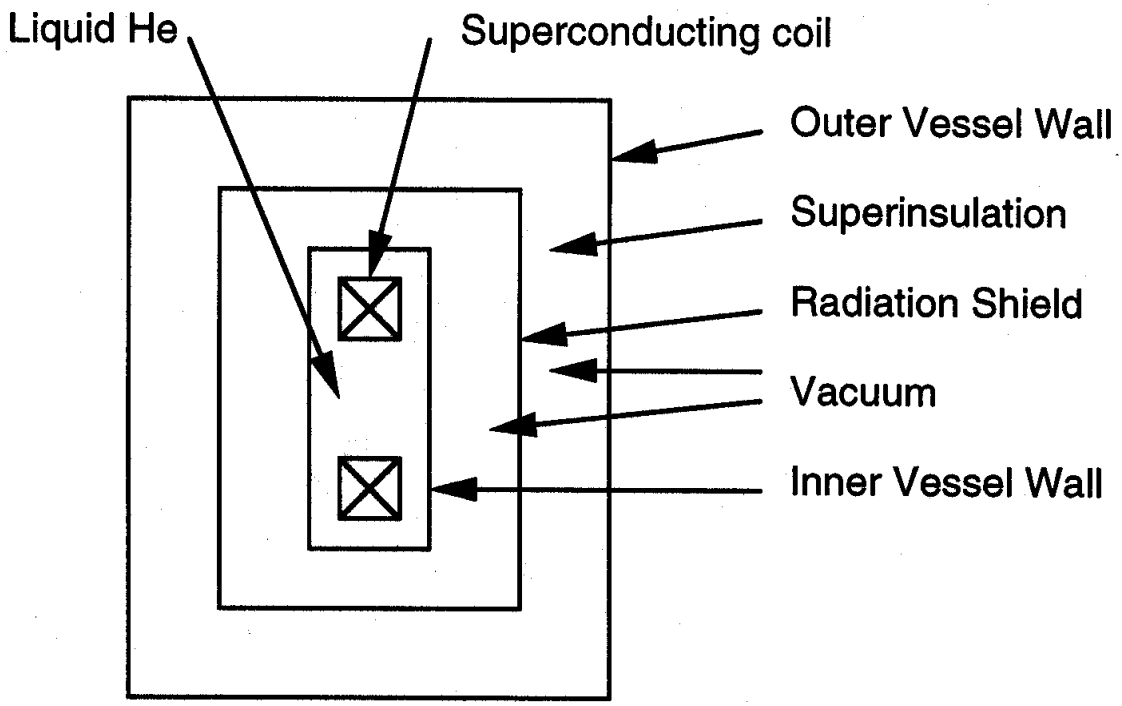

Figure 3 Cross Section of a Superconducting Magnet

the superconductor winding and liquid helium, is enclosed in a vacuum chamber, which, in turn, rests within an evacuated but insulation-filled chamber surrounded by an outer wall. The middle chamber walls , which are liquid-nitrogen cooled, are referred to as radiation shields. The outer most vessel walls, generally the most thick, serve as eddy current shields. Considerable attention as been devoted to the design of SCM's for maglev applications in Japan[26, 31-36] and elsewhere, and also to the heating effects of eddy currents induced in the cryostat walls[6, 32, 33].

Depending on the materials used in the walls, their thickness, and the frequency of the applied fields to which they are exposed, time varying fields may penetrate one, two or even all three vessel walls and reach the windings were they will induce eddy currents that could lead to a magnet quench (i.e., loss of the superconducting state). In the important frequency range of 1 to 10 Hz, corresponding to most vehicle vibration modes, the eddy current losses tend to decrease from the outer to the inner vessel walls[6]. For computational simplicity, it will be assumed here that all significant losses occur in the vertical outer wall. This ignores eddy current losses in the top, bottom, and end surfaces as well as the inner vessel walls. However, this will be sufficient for the purposes of comparing different damping mechanisms. More will be said about this simplification in Sec. 6.

A further simplification is to replace each metallic plate serving as a damping plate with one or two "equivalent" damping coils. These "equivalent" damping coils are assumed to be shorted, single-turns in the same plane as the plates and made of the same material. The dimensions of the "equivalent" damping coils are difficult to determine precisely, but they are important for accurate calculations of damping coefficients. As a first approximation[*], for purposes of comparing the effectiveness of different mechanisms, it will suffice to use the same thickness as the plates and coil shapes that closely resemble the shapes of the coils that serve as the field sources that cause the eddy currents. For example, if the null-flux coils are the field source, then the damping coils are in the plane of the outer cryostat walls and consist of two separate coils, each one facing the corresponding upper or lower loop of the null-flux coil. In this configuration, the direction of the eddy currents in the upper damping coil is opposite to that in the lower damping coil. If the propulsion coil is the field source, then the most reasonable choice would be to use a single damping coil whose shape reflects that of the propulsion coil. In both cases, it is assumed that each SCM winding and its corresponding cryostat wall spans three null-flux coils and three propulsion coils as illustrated in Fig. 1. [This choice corresponds to the Japanese repulsive force maglev system being developed and tested at the Yamanashi test track. There, four SC windings are placed on one side of a bogie and all four share an outer cryostat wall in common. It should be noted that the system tested at the Miyazaki test track used a similar configuration but with three SC windings, i.e. three magnetic poles per bogie.]

[*] See Sec. 6 for an analysis of the sensitivity of the damping coefficients to the choice of the damping coil dimensions

Fig. 4 shows the cross-sectional view of a SCM winding, an outer cryostat wall, a null-flux lift coil, and a propulsion coil. Fig. 5 shows a facing view of the guideway lift and propulsion coils and the corresponding equivalent damping coils used to simulate the damping effects of the outer cryostat walls fixed to the vehicle.

4.1 Theoretical Model of Passive Damping Due to Eddy Currents Induced in Damping Plates by Motion Relative to the Null-Flux Lift Coils.

The coil configuration being examined in this section is illustrated in Fig. 5. The method of analysis used here is based on the dynamic circuit model described in Ref. 3. A similar method was reported earlier in Ref. 4.

Applying Kirchhoff's voltage law to the four electrical circuits equivalent to the upper and lower loops of a null-flux coil and the upper and lower damping loops, respectively , results in the following four voltage equations:

$$i_{gu}R_{gu} + \frac{d\phi_{gu,g}}{dt} + \frac{d\phi_{gu,d}}{dt} + \frac{d\phi_{gu,s}}{dt} = 0, \tag{9a}$$

$$i_{gl}R_{gl} + \frac{d\phi_{gl,g}}{dt} + \frac{d\phi_{gl,d}}{dt} + \frac{d\phi_{gl,s}}{dt} = 0, \tag{9b}$$

$$i_{du}R_{du} + \frac{d\phi_{du,d}}{dt} + \frac{d\phi_{du,g}}{dt} = 0, \textit{and} \tag{9c}$$

$$i_{dl}R_{dl} + \frac{d\phi_{dl,d}}{dt} + \frac{d\phi_{dl,g}}{dt} = 0, \tag{9d}$$

where i is the current, R is the resistance, and ϕ is the flux linkage. The flux linkages are classified based on their generating sources. $\phi_{gu,g}$ and $\phi_{gl,g}$ are the flux linkages of the upper and lower loops of a null-flux coil with themselves and with neighboring null-flux coil loops. Similarly, $\phi_{gu,d}$ and $\phi_{gl,d}$ are the flux linkages with the damping coils; $\phi_{gu,s}$ and $\phi_{gl,s}$ are the flux linkages with the SCM; $\phi_{du,d}$ and $\phi_{dl,d}$ are the flux linkages with themselves and neighboring damping loops; and $\phi_{du,g}$ and $\phi_{dl,g}$ represent the flux linkages with all the null-flux coils. ["g" stands for ground or null-flux coils, "d" for damping coil, and "s" for SCM or superconducting magnet coil] [Note that, because of the null-flux arrangement, the null-flux and propulsion coils do not interfere with each other. Higher order transient effects between these coils are ignored.]

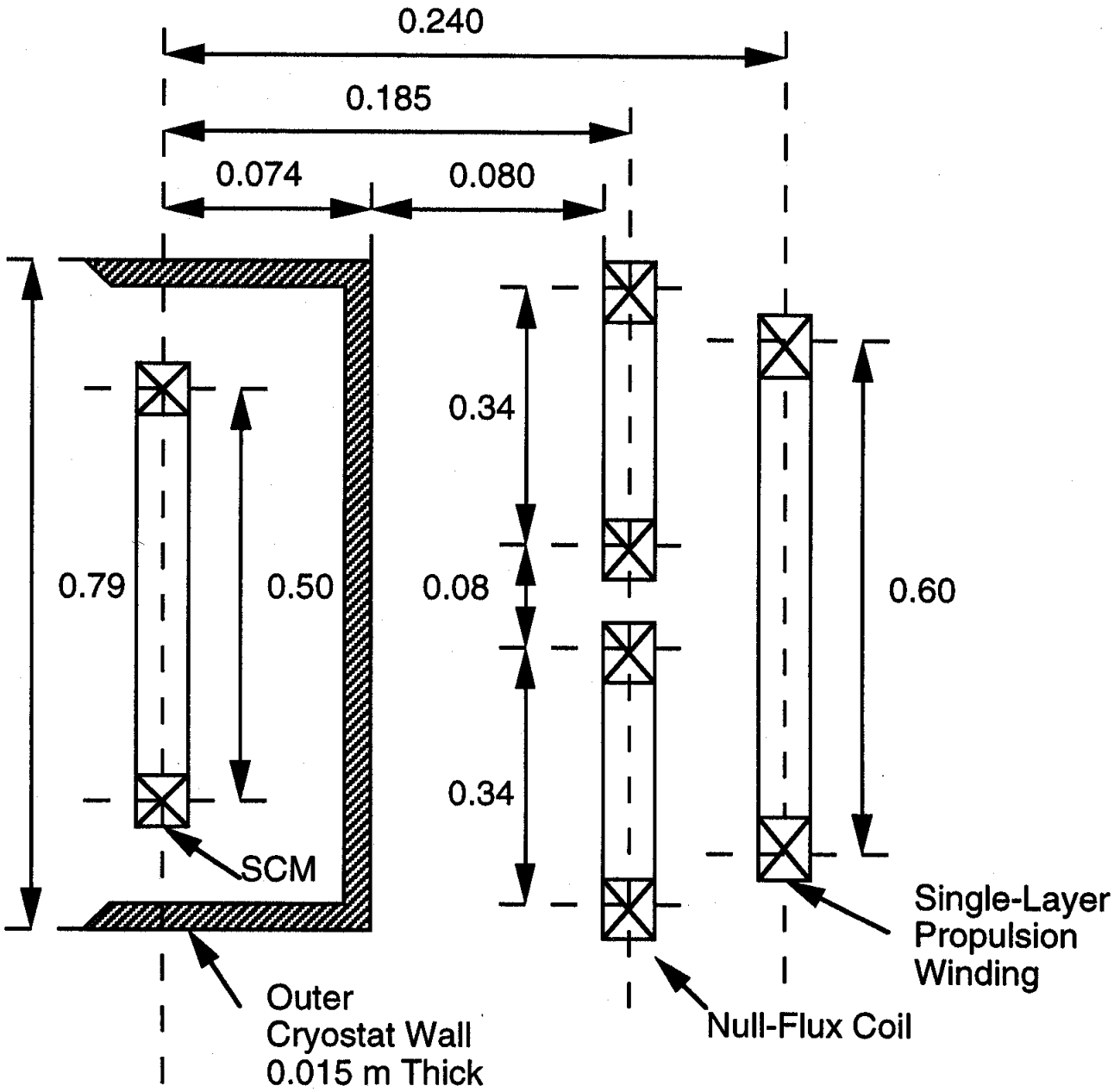

Figure 4 Cross Sectional View of Coil System Being Analyzed

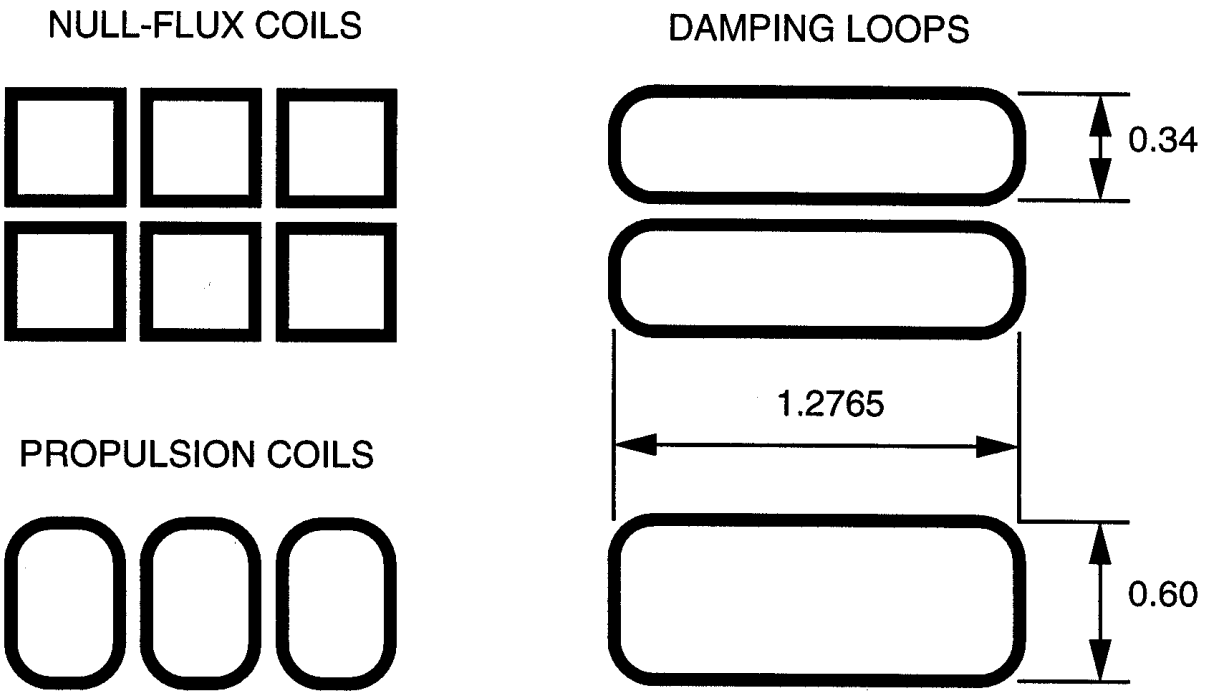

Figure 5. Shorted, Single-turn Damping Coils Used to Simulate Damping Action of Damping Plate or Outer Cryostat Wall. For a Null-Flux Coil, an Upper and Lower Damping Coil is Used. For a Propulsion Coil, a Single Damping Coil is Used.

The dominant terms in Eqns. (9a) and (9b) are the fourth terms, which represent the voltages induced in the null-flux loops by an SCM moving longitudinally along the guideway. They give rise to the lift forces. The smallest terms are the voltages induced in the null-flux loops by eddy currents circulating in the damping loops. The latter voltages are second order and can be neglected. To a good approximation, the periodic magnetic field seen by the null-flux loops as they move longitudinally relative to the SCM's can be represented by the fundamental term in a Fourier series. Consequently, the resulting flux linkages are given approximately, by

$$\phi_{gu,s} = I_s M_{gu.s}(y,z)\sin\beta x \quad \text{and} \tag{10}$$

$$\phi_{gl,s} = I_s M_{gl.s}(y,z)\sin\beta x\,, \tag{11}$$

where I_s is the SCM current, assumed to be constant, the *M's* are the mutual inductances between the SCM and the upper and lower loops of the null-flux coil, respectively, and $\beta = \pi/p$, where p is the pole pitch of the SCM coils.

Since the upper and lower loops of the null-flux coil are cross connected, the currents flowing in them are equal in magnitude but opposite in sign. That is,

$$i_{gu} = -i_{gl} = i_g \tag{12}$$

In addition, since the null-flux coil resistance is expected to be much smaller than its inductive reactance, that is.

$$R_g << X_g\ (=\omega L), \tag{13}$$

it follows that Eqn. (9b) can be subtracted from Eqn. (9a) and reduced as follows:

$$\frac{d}{dt}i_g = \frac{1}{2\left(L_g - M_{gu,gl}\right)}\frac{d}{dt}\left(\phi_{gl,s} - \phi_{gu,s}\right) \tag{14a}$$

$$\frac{d}{dt}i_g = \frac{1}{2\left(L_g - M_{gu,gl}\right)}\overline{V.\nabla}\left(\phi_{gl,s} - \phi_{gu,s}\right) \tag{14b}$$

$$\frac{d}{dt}i_g \approx \frac{1}{2\left(L_g - M_{gu,gl}\right)}v_x\frac{\partial}{\partial x}\left(\phi_{gl,s} - \phi_{gu,s}\right), \tag{14c}$$

where the terms involving components of the velocity in the y and z direction have been ignored because they are small relative to the longitudinal component v_x. Substituting Eqns. (10) and (11) into Eqn. (14c) yields

$$\frac{d}{dt} i_g = \frac{I_s}{2\left(L_g - M_{gu,gl}\right)} v_x \beta \left(M_{gl,s} - M_{gu,s}\right) \cos \beta x \,. \tag{15}$$

Now since $x = v_x t$, and $\beta = \pi/p = 2\pi/\lambda$, it follows that $\beta x = 2\pi v_x t/\lambda = \omega t$, and

$$i_g = \frac{I_s}{2\left(L_g - M_{gu,gl}\right)} \left(M_{gl,s} - M_{gu,s}\right) \sin \omega t \,. \tag{16}$$

Hence, the peak value of the current in the null-flux loops is given by

$$I_{gm} = \frac{I_s}{2\left(L_g - M_{gu,gl}\right)} \left(M_{gl,s} - M_{gu,s}\right). \tag{17}$$

Now, since one SCM and its corresponding section of cryostat wall spans three null-flux coils, the flux linking the null-flux coils to the upper and lower damping loops can be expressed as the sum of the contributions from each of the three corresponding null-flux loops as follows:

$$\phi_{du,g} = i_{g-1} M_{du,gu-1} + i_g M_{du,gu} + i_{g+1} M_{du,gu+1} \text{ , and} \tag{18}$$

$$\phi_{dl,g} = -i_{g-1} M_{dl,gl-1} - i_g M_{dl,gl} - i_{g+1} M_{dl,gl+1} \text{ ,} \tag{19}$$

where i_{g-1} , i_g , and i_{g+1} are the currents flowing in the first, second, and third null-flux coils facing the damping loops, respectively, and $M_{du,gu-1}$, $M_{du,gu}$, and $M_{du,gu+1}$ are the mutual inductances between the upper damping loops and the upper loops of the first, second, and third facing null-flux coils, respectively. The flux linkages between the upper damping loops and the lower null-flux loops and vice verse are ignored. The mutual inductances between the upper and lower damping loops are also ignored.

Using a harmonic approximation, the currents induced in the three null-flux loops facing a single SCM are each delayed by one-third of a time period. The mutual inductance terms are similarly delayed by one-third of a pole pitch. Consequently, using some trigonometric identities, it is easily shown that the summations given in Eqns. (18) and (19) can be rewritten as traveling waves of the form

$$\phi_{\mathrm{d,g}} = \phi_{du,gu} = -\phi_{dl,gl} = \frac{3}{2} I_{gm} M_{d,g}(y,z)\sin(\omega_x t - \beta_x x)\,, \tag{20}$$

where I_{gm} is given by Eqn. 17, $M_{d,g}$ is the y and z-dependent part of mutual inductance between a null-flux loop and its facing damping loop, and $\beta_x = \pi/p$. Eqn. (20) shows that the flux linkage between the three null-flux coils and the facing damping loop travels along with the damping loop at the longitudinal speed v_x. Consequently, the damping loop sees a value of flux linkage that is independent of its longitudinal position along the guideway. This simplification permits the separation of the constant-speed motion in the x-direction from any disturbances in the y and z-directions.

The average power dissipated in one of the damping loops can be expressed as

$$P_d = \left\langle i_d^*(t) i_d(t) \right\rangle_{rms} R_d = \frac{\left\langle \varepsilon_d(t) \right\rangle_{rms}^2 R_d}{R_d^2 + X_d^2}\ , \tag{21}$$

where ε_d(t) is the voltage induced in the damping loop, and R_d and X_d are the resistance and reactance of the damping loop. Assuming a harmonic approximation, and harmonic motion in only the y or z direction, the induced voltage is given by

$$\left\langle \varepsilon_d(t) \right\rangle_{rms} = -\left\langle \frac{d}{dt}\phi_{d,g} \right\rangle_{rms} = -\left\langle \vec{v}.\vec{\nabla}\phi_{d,g} \right\rangle_{rms} \tag{22}$$

$$= V_z \frac{\partial}{\partial z}\phi_{d,g}\ , \tag{23}$$

or

$$= V_y \frac{\partial}{\partial y}\phi_{d,g}\ , \tag{24}$$

where V_z and V_y are the rms values of the velocities in the z and y-directions, and Eqns. (23) and (24) are used for motion in the z and y-directions, respectively. Now, using the amplitude of the flux linkage from Eqn. (20) together with the expression for the rms voltage, Eqn. (23), the average dissipated power in a damping loop associated with motion in the z-direction is given by

$$P_{dz} = \frac{R_d}{R_d^2 + X_d^2} V_z^2 \frac{9}{4}\left[\frac{\partial}{\partial z}(I_{gm} M_{d,g})\right]^2. \tag{25}$$

Substituting the expression for I_{gm} from Eqn. (17) ,

$$P_{dz} = \frac{9}{16}\frac{R_d}{R_d^2 + X_d^2} V_z^2 I_s^2 \left\{ \frac{1}{L_{geff}} \frac{\partial}{\partial z} \left[(M_{gl,s} - M_{gu,s}) M_{d,g} \right] \right\}^2 , \tag{26}$$

where $L_{g\,eff} = L_g - M_{gl,gu}$ This expression can be written in a more convenient form by defining a critical frequency

$$f_c = \frac{R_d}{2\pi L_d} . \tag{27}$$

After some manipulation,

$$P_d = \frac{9}{16}\frac{V_z^2 I_s^2}{R_d}\frac{1}{1+\left(\frac{f_z}{f_c}\right)^2} \left\{ \frac{1}{L_{geff}} \frac{\partial}{\partial z} \left[(M_{gl,s} - M_{gu,s}) M_{d,g} \right] \right\}^2 . \tag{28}$$

From Eqn. (28) we can identify the damping coefficient for motion in the z-direction as

$$C_z = P_d / V_z^2 , \tag{29}$$

and the normalized vertical damping coefficient for one damping loop is given by

$$C_z^n = \left[1 + \left(\frac{f_z}{f_c}\right)^2 \right] C_z = \frac{9}{16}\frac{I_s^2}{R_d} \left\{ \frac{1}{L_{geff}} \frac{\partial}{\partial z} \left[(M_{gl,s} - M_{gu,s}) M_{d,g} \right] \right\}^2 \tag{30}$$

The corresponding expression for the normalized lateral damping coefficient is given by

$$C_y^n = \left[1 + \left(\frac{f_y}{f_c}\right)^2 \right] C_y = \frac{9}{16}\frac{I_s^2}{R_d} \left\{ \frac{1}{L_{geff}} \frac{\partial}{\partial y} \left[(M_{gl,s} - M_{gu,s}) M_{d,g} \right] \right\}^2 \tag{31}$$

It should be noted that the frequency-dependence of the damping coefficients is included in the normalization factors in Eqns. (30) and (31). This is a consequence of the use of the harmonic approximation for the current in the null-flux and damping loops. This frequency dependence is illustrated in Fig. 6. The same critical frequency applies to both the vertical and lateral normalization factors. It is dependent on the ratio of equivalent values of R_d and L_d of the damping coil used to simulate the effect of the damping plate.

In order to examine the damping coefficients, the term inside the curly brackets in Eqn. (30) can be expanded to

$$\frac{1}{L_{geff}}\left\lfloor \frac{\partial}{\partial z}(M_{gl,s} - M_{gu,s})M_{d,g} + (M_{gl,s} - M_{gu,s})\frac{\partial}{\partial z}M_{d,g}\right\rfloor \tag{32}$$

with a similar expression for the y-direction. At the null-flux position, $M_{gl,s} = M_{gu,s}$ so that the second term in Expression (32) vanishes. However, as is characteristic of null-flux systems, the derivative with respect to z of $(M_{gl,s} - M_{gu,s})$ is at a maximum at that position. Hence the first term is large and the damping in the z-direction is large. On the other hand, the derivative with respect to y of $(M_{gl,s} - M_{gu,s})$ is zero by symmetry, so that there is no damping of lateral motion at the null-flux position. As the vertical offset increases, both the first and second terms in Expression (32) contribute to the damping in both the y and z-directions.

It should be noted that, if the vertical offset from the neutral position of the null-flux coil is relatively small, compared to the height of the damping loops, the upper and lower damping loops will have essentially the same damping coefficients. However, if the vertical offset is large, or the height of the damping loops is relatively small, then vertical symmetry will be lost and it will be necessary to compute the damping coefficient for each damping loop separately.

For purposes of making a consistency check later on, the maximum value of the lift force for a null-flux coil can be expressed in terms already defined above as

$$F_l = I_{gm} I_s \frac{\partial}{\partial z}\left(M_{gl,s} - M_{gu,s}\right) . \tag{33}$$

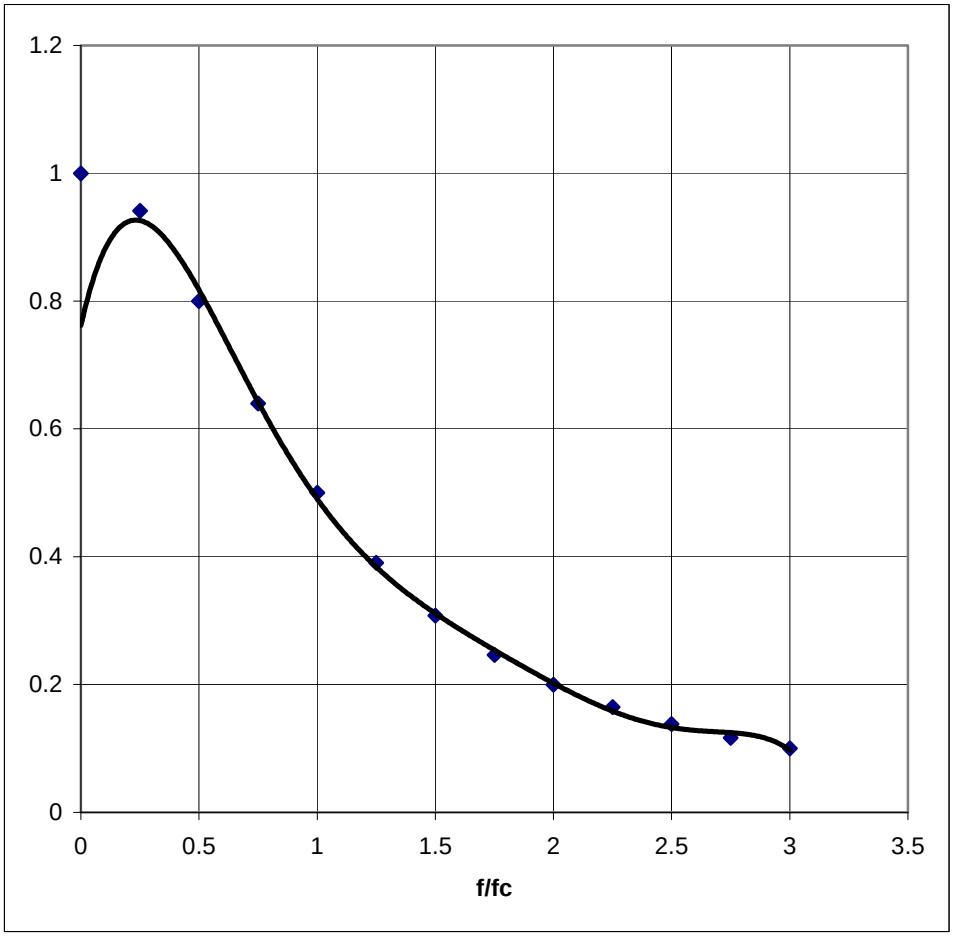

Figure 6 Damping Coefficient Normalization Factor

4.2 Results of Calculations of Damping Caused by Eddy Currents Induced in Damping Coils by the Null-Flux Coils.

The parameter values used in the calculations described below are listed in Table 5. These values apply approximately to the Yamanashi test vehicles and guideway.

Fig. 7a shows the mutual inductance between the lower and upper loops of a null-flux coil and the SCM as a function of the vertical offset from the neutral position, i.e., the point midway between the upper and lower loops. [Computations of mutual inductance use a numerical computer code based on the formulae given in Ref. 37.] Negative values of the vertical offset correspond to the normal case of magnetic levitation where center of the vehicle-borne SCM's are below the neutral position of the null-flux coils. As the vertical offset increases from a negative value, the SCM becomes less aligned with the lower loop and the mutual inductance decreases almost linearly. The derivative with respect to the vertical offset *(∂/∂z)* is negative and almost constant. At the neutral position, the mutual inductances between the upper and lower loops and the SCM are equal and their derivatives are equal in magnitude but opposite in sign. Fig. 7b shows the differences between these mutual inductances and the differences between their derivatives with respect to z. Fig. 8 shows the mutual inductance and its derivative with respect to z between a null-flux coil and a damping coil. The mutual inductance is maximum at the neutral position and its derivative is zero there. Reference to Expression 32, shown below for convenience,

$$\frac{1}{L_{geff}}\left[\frac{\partial}{\partial z}(M_{gl,s}-M_{gu,s})M_{d,g}+(M_{gl,s}-M_{gu,s})\frac{\partial}{\partial z}M_{d,g}\right] \tag{32}$$

indicates how the various mutual inductance terms and their derivatives contribute to the vertical damping coefficient. For example, at the null-flux position, the second term vanishes because the two mutual inductances are equal. The first term, on the other hand, makes its maximum contribution because the difference in the derivatives is at a maximum value at that point, as is the mutual inductance between the null-flux loop and the damping loop.

Consequently, this mechanism provides maximum damping in the vertical direction in the neutral position as shown in Fig. 9. At speeds below liftoff, where the vehicle is supported near the neutral position by the landing gear (to minimize drag), or at very high speed, where the vertical offset is relatively small, the vertical damping coefficient for this mechanism is relatively large. At intermediate speeds, where the vertical offset is larger, the vertical damping coefficient is smaller.

Table 5 Parameter Values Used in Damping Calculations

	SCM Winding	Outer Cryostat Wall	Null-Flux Coil Loop	Simulated Damping Loop	Propulsion Coil Loop	Simulated Damping Loop
Length, X-Dir.	1.07	5.4	0.350	1.2765	0.3364	1.2765
Height, Z-Dir.	0.5	0.79	0.340	0.34	0.6	0.6
Thickness, Y-Dir.		0.015	0.038	0.015	0.0368	0.015
Width, XZ plane			0.079	0.079	0.0735	0.079
Winding Cross Sec.			0.003	0.0012	0.0027	0.0012
Series Turns			24	1	8	1
Parallel Windings			2			
Vertical spacing			0.080			
Horizontal Spacing			0.100			
Pole Pitch	1.35				1.35	
Conductivity (S/m)				3.53E+07	3.53E+07	3.53E+07
Resistance (m Ω)			8.34	0.0773	1.4	0.0897
Self Inductance (mH)			0.4054	0.00191	0.06398	0.002458
U-L Mutual Ind. (mH)			-0.0212			
Excitation (kA)	700				1.188	
Damping Coil Crit. Freq.*				6.4412		5.80806

*Sensitive to dimensions of coil used to simulate damping effects of damping plate
Coil dimensions are center-to-center of windings

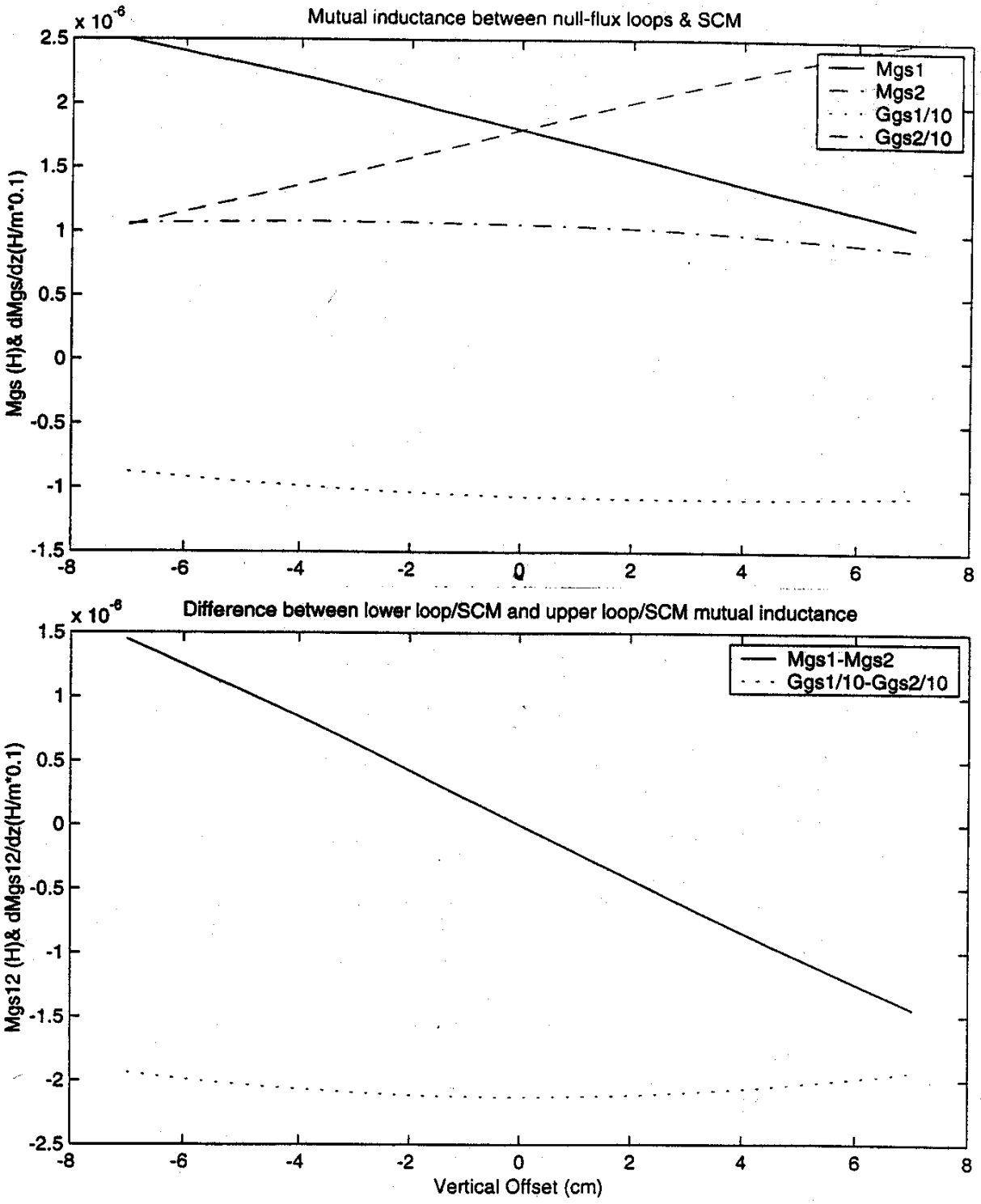

Figure 7. a) (upper graph) Mutual Inductance Between the Upper and Lower Null-Flux Loops and the SCM as a Function of the Vertical Offset: b) (lower graph) Differences Between These Mutual Inductances and the Differences Between Their Derivatives With Respect to z.

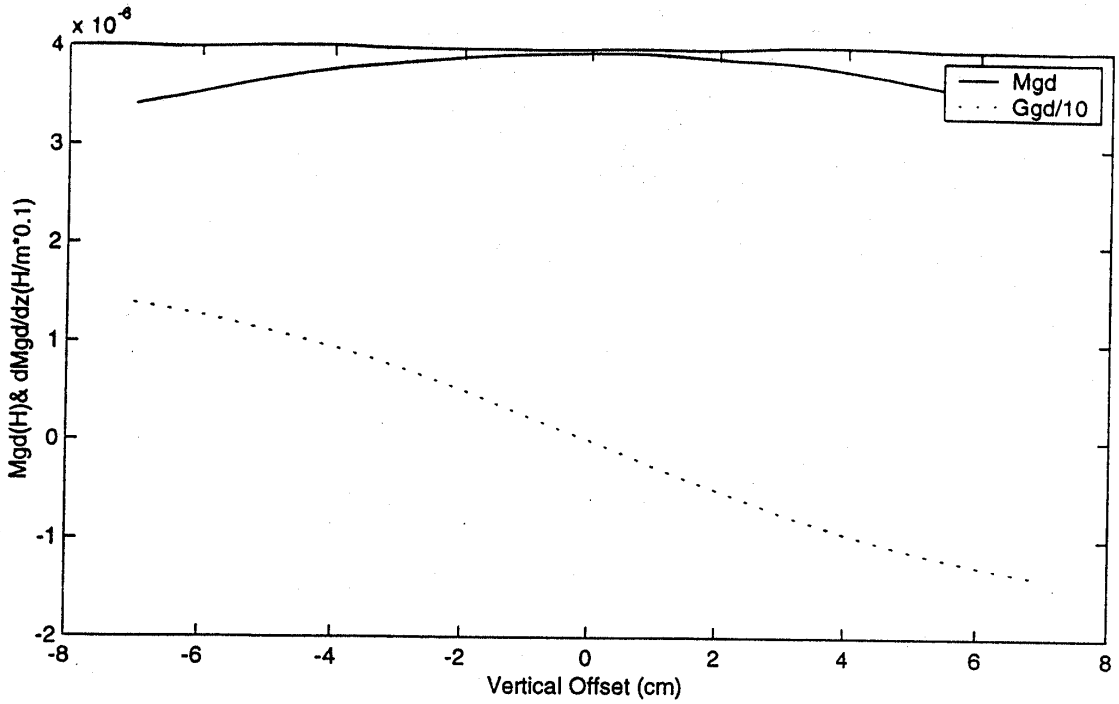

Figure 8. The Mutual Inductance and Its Derivative With Respect to z Between a Null-Flux Coil Loop and the Facing Damping Coil.

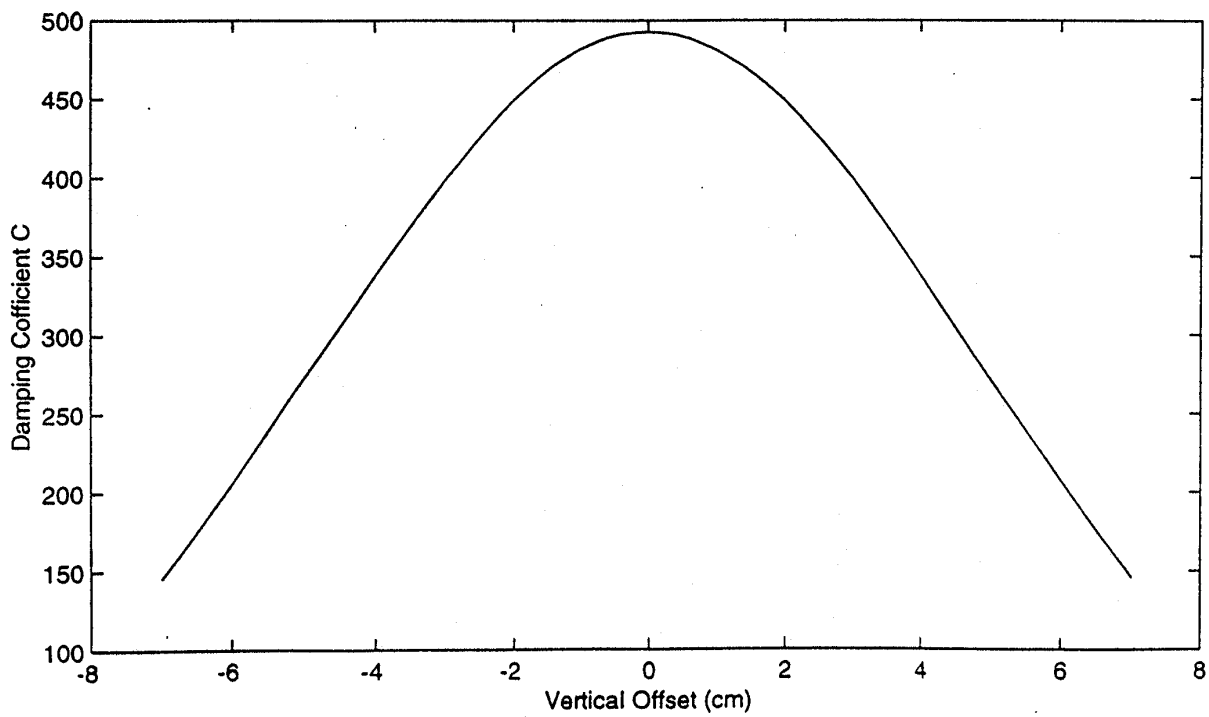

Figure 9. Null-Flux – Damping Loop Normalized Vertical Damping Coefficient

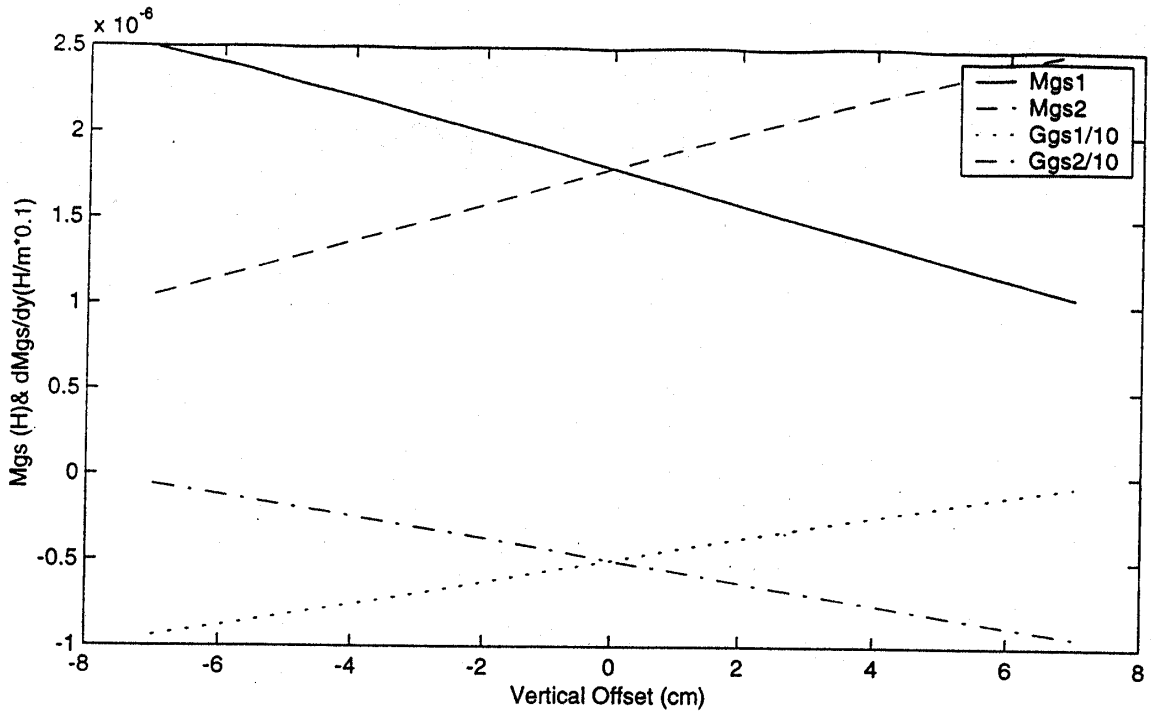

Figure 10. Mutual Inductances and its Derivatives With Respect to y Between the Upper and Lower Null-Flux Loops and the SCM.

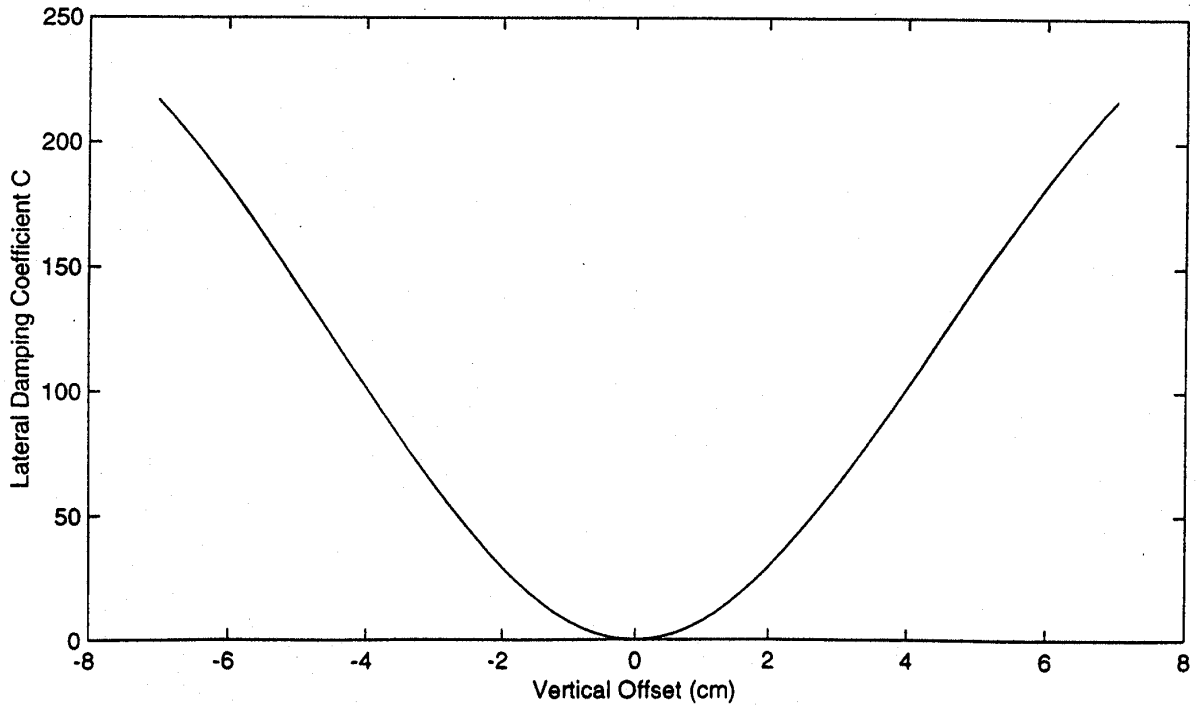

Figure 11. Null-Flux – Damping Loop Normalized Lateral Damping Coefficient

These results can be compared with those for the lateral damping coefficient. Fig. 10 shows the mutual inductance between the upper and lower loops of the null-flux coil and the SCM and its derivative with respect to the lateral direction *(∂/∂y)* as a function of vertical offset. Whereas the mutual inductances are the same as above, the derivatives have the same sign. In contrast to the above result, this difference causes the function that couples the null-flux, SCM and damping coil to vanish at the neutral position [see Expression (32) with the *(∂/∂z)*'s replaced by *(∂/∂y)*'s] . That is, this mechanism produces zero damping in the lateral direction at the neutral position, but the lateral damping coefficient increases with vertical offset as shown in Fig. 11. Hence, at speeds below liftoff, where the vehicle is supported near the neutral position by the landing gear, this mechanism produces no lateral damping. At very high speed, where the vertical offset is relatively small (≈ 3 to 4 cm), the lateral damping coefficient for this mechanism is smaller than the vertical damping coefficient. At intermediate speeds where the vertical offset is relatively large, the lateral damping produced by this mechanism is stronger, but still weaker than the vertical damping coefficient.

5. Passive Damping Due to Eddy Currents Induced in Damping Plates by Motion Relative to the Propulsion Coils

Another contribution to the time varying component of the magnetic field seen by the vehicle-borne conductors is caused by the three-phase excitation of the propulsion coils. That excitation produces a fundamental travelling magnetic wave that travels at the synchronous velocity ($v_x = 2pf$) and harmonic waves of reduced amplitude that travel at higher speeds. Since the vehicle travels at the synchronous velocity, the fundamental is at rest relative to the vehicle conductors. However, if the vehicle moves relative to the synchronous velocity, currents will be induced in the vehicle conductors.

It should be noted that since the harmonic traveling magnetic waves are moving relative to the vehicle conductors, they will induce eddy currents in the vehicle conductors even if the vehicle does not move relative to the synchronous velocity. However,these eddy currents do not contribute to damping. Only those eddy currents attributable to the unwanted motion contribute to damping. The damping of the unwanted motions caused by the harmonics are presumed to be small compared to that associated with the fundamental traveling wave because of the magnitudes of the currents involved. Only the damping associated with motions related to the fundamental synchronous velocity will be evaluated here. The effects of the harmonics are ignored.

5.1 Theoretical Model of Passive Damping Due to Eddy Currents Induced in Damping Coils by Motion Relative to the Propulsion Coils

This model is very similar to that of Subsection 4.1. The principal difference is that whereas the current in the null-flux coils is induced by motion relative to the SCM's, and depends on the derivatives of the mutual inductance between the null-flux coil loops and the SCM coils, the current in the propulsion coils is the net result of the induced electromotive force and the voltage applied by an external three-phase power source. This difference results in a substantial simplification of the expressions for the damping coefficients. Again, applying Kirchhoff's law, we have the following two voltage equations to deal with:

$$i_p R_p + \frac{d\phi_{p,p}}{dt} + \frac{d\phi_{p,s}}{dt} + \frac{d\phi_{p,d}}{dt} = E_a \text{, and} \tag{34a}$$

$$i_d R_d + \frac{d\phi_{d,d}}{dt} + \frac{d\phi_{d,p}}{dt} = 0 \text{,} \tag{34b}$$

where Eqn. (34a) applies to the equivalent circuit of one phase of the linear propulsion winding, E_a is the applied phase voltage, and the flux linkages $\phi_{p,p}$, $\phi_{p,s}$, and $\phi_{p,d}$ are due to the self inductance of the propulsion coils, the mutual inductance with the SCM coils, and the mutual inductance with the damping loops, respectively. The fourth term in Eqn. (34a) is much smaller than the second and third terms and can be ignored. Eqn. (34b) applies to the damping loops.

As a further simplification, we will take the current flowing in the propulsion windings (I_p) as a given. A value should be chosen that is consistent with propulsion requirements. This leaves only one voltage equation, Eqn. (34b), to be solved for the current flowing through the damping loop. Since the propulsion windings are excited with three-phase power, each set of three propulsion coils constitutes a single magnetic pole that travels along with the facing SCM coil and its section of cryostat wall. Consequently, it is reasonable to simulate that section of co-moving cryostat wall as a shorted, single-turn loop as illustrated in Fig. 5.

As in the case of the null-flux coils, the flux linking the three propulsion coils to a single damping loop can be written as

$$\phi_{d,p} = \frac{3}{2} I_p M_{d,g}(y,z)\sin(\omega_x t - \beta_x x) \text{,} \tag{35}$$

where, as before, $\beta_x = \pi/p$, and $\omega = \pi v_x/p$

The average power dissipated in a damping loop facing a set of three propulsion windings is given by

$$P_{dp} = \left\langle i_{dp}^*(t) i_{dp}(t) \right\rangle_{rms} R_{dp}$$

$$= \frac{\left\langle \varepsilon_{dp}(t) \right\rangle_{rms}^2 R_{dp}}{R_{dp}^2 + X_{dp}^2} \tag{36}$$

Following the same derivation as in the previous subsection, but recognizing that the propulsion current is only very weakly dependent on z and y, the dissipated power for motions in the z and y-directions is given by

$$P_{dpz} = \frac{R_{dp}}{R_{dp}^2 + X_{dp}^2} I_p^2 V_z^2 \frac{9}{4} \left[\frac{\partial}{\partial z} (M_{d,p}) \right]^2, \qquad \text{and} \tag{37}$$

$$P_{dpy} = \frac{R_{dp}}{R_{dp}^2 + X_{dp}^2} I_p^2 V_z^2 \frac{9}{4} \left[\frac{\partial}{\partial y} (M_{d,p}) \right]^2, \tag{38}$$

Again, introducing the critical frequency

$$f_{cp} = \frac{R_{dp}}{2\pi L_{dp}} \ , \tag{39}$$

the normalized damping coefficients in for the z and y-directions are given by

$$C_{zp}^n = \left[1 + \left(\frac{f_z}{f_{cp}} \right)^2 \right] C_{zp} \ , \text{ and} \tag{40}$$

$$C_{yp}^n = \left[1 + \left(\frac{f_z}{f_{cp}} \right)^2 \right] C_{yp} \ , \tag{41}$$

where

$$C_{zp} = \frac{9}{16}\frac{I_p^2}{R_{dp}}\frac{1}{1+\left(\frac{f_z}{f_{cp}}\right)^2}\left[\frac{\partial}{\partial z}M_{d,p}\right]^2 \tag{42}$$

$$C_{yp} = \frac{9}{16}\frac{I_p^2}{R_{dp}}\frac{1}{1+\left(\frac{f_y}{f_{cp}}\right)^2}\left[\frac{\partial}{\partial y}M_{d,p}\right]^2 . \tag{43}$$

5.2 Results of Calculations of Damping Caused by Eddy Currents Induced in the Damping Coils by the Propulsion Coils.

The mutual inductance between a propulsion coil and a damping coil used to simulate a damping plate is shown in Fig. 12 as a function of the vertical offset. The derivative of the mutual inductance with respect to z, is also shown in that figure. It is seen that, at the neutral position, the mutual inductance passes through a peak value, whereas the derivative with respect to z passes through zero. Consequently, the vertical damping coefficient for this mechanism is zero at the neutral position and increases as the vertical offset increases as shown in Fig. 13. However, the magnitude of this damping coefficient is four orders of magnitude smaller than for the null-flux case described in Sec. 4.1 (see Fig. 9). Hence, this mechanism contributes very little to the overall passive vertical damping of the system.

Fig. 14 shows the mutual inductance, and its derivative with respect to y, between a propulsion coil and a damping coil. Since the derivative with respect to y is an order of magnitude larger than with respect to the vertical direction, the lateral damping coefficient is also an order of magnitude larger. In addition, because the derivative with respect to y is slightly peaked near the neutral position, the lateral damping coefficient is also at a maximum value as indicated in Fig. 15. Hence this mechanism does make a contribution to the lateral damping at the neutral position, but it is still quite small relative to the null-flux coil mechanism even at small but non-zero vertical offsets (see Fig. 11).

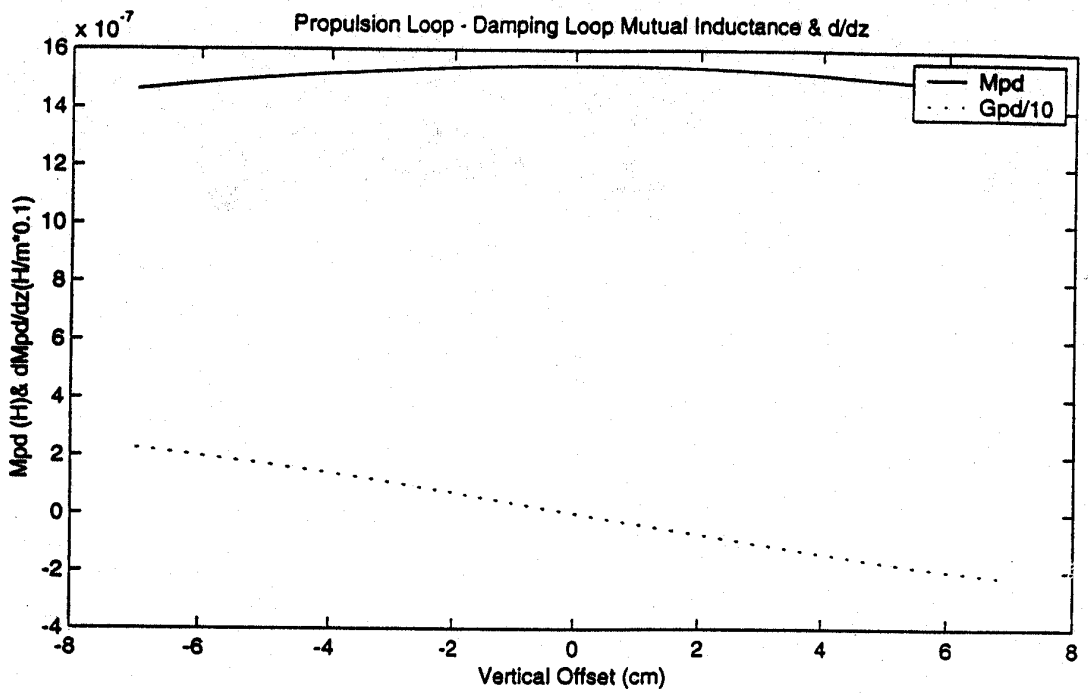

Figure 12. Mutual Inductance and its Derivative With Respect to z Between a Propulsion Coil and the Facing Damping Loop as a Function of the Vertical Offset.

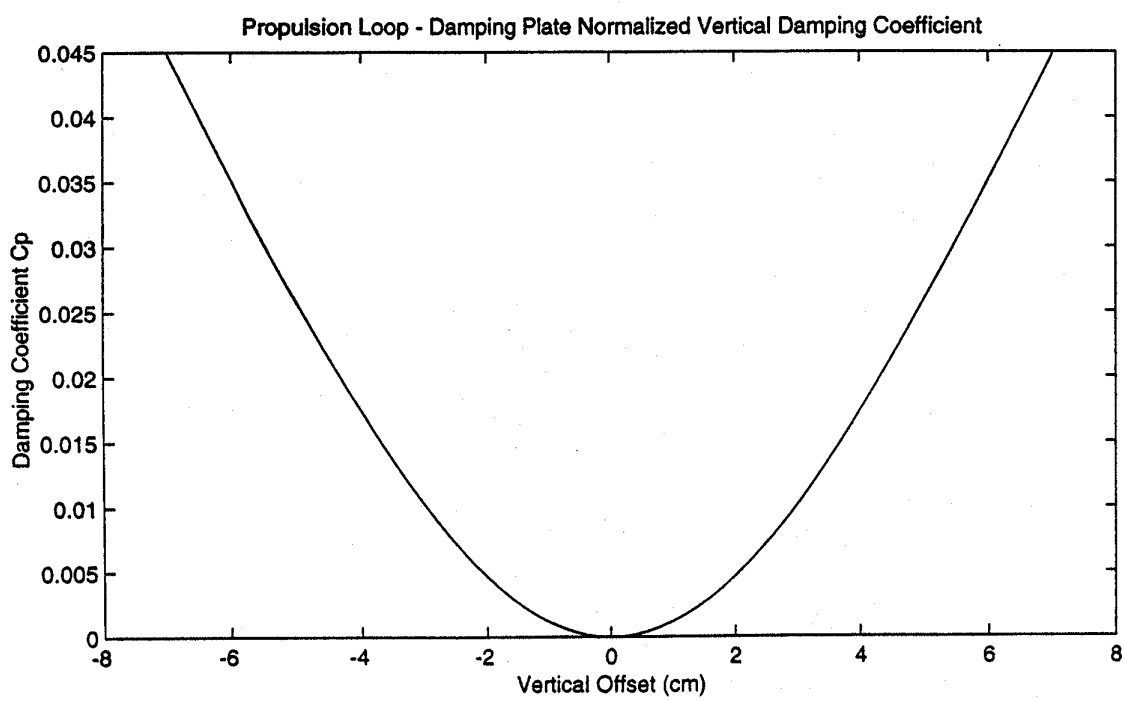

Figure 13. Propulsion Coil – Damping Coil Normalized Vertical Damping Coefficient

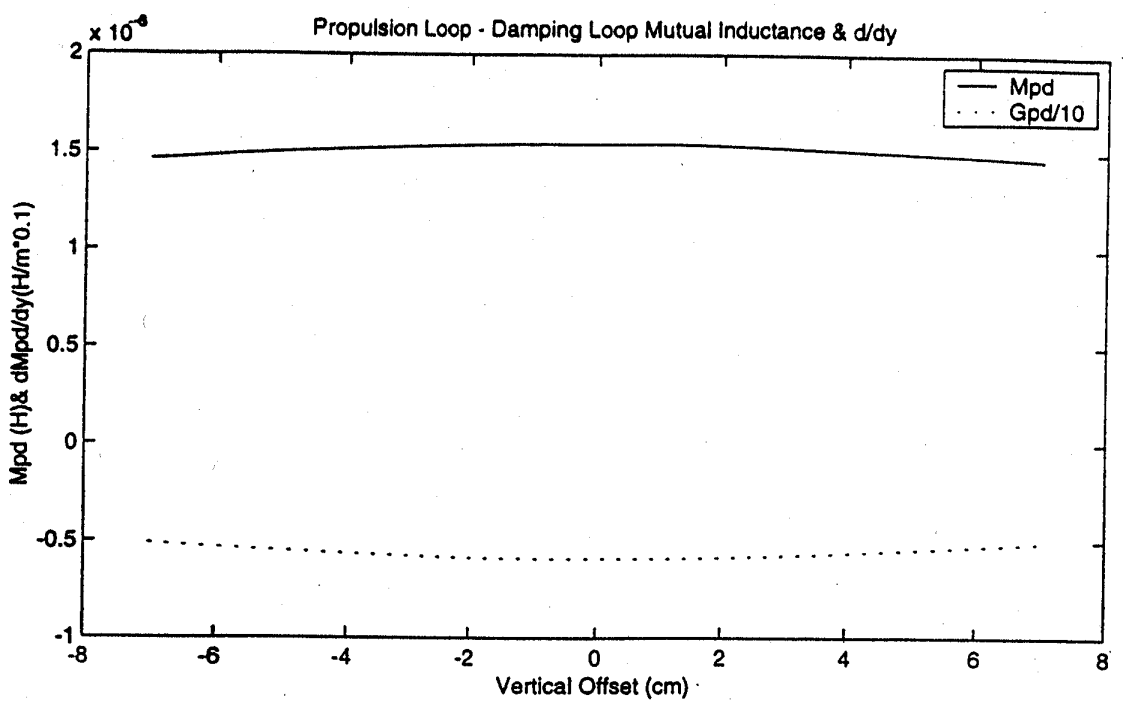

Figure 14. Mutual Inductance and its Derivative With Respect to y Between a Propulsion Coil and the Facing Damping Loop as a Function of the Vertical Offset.

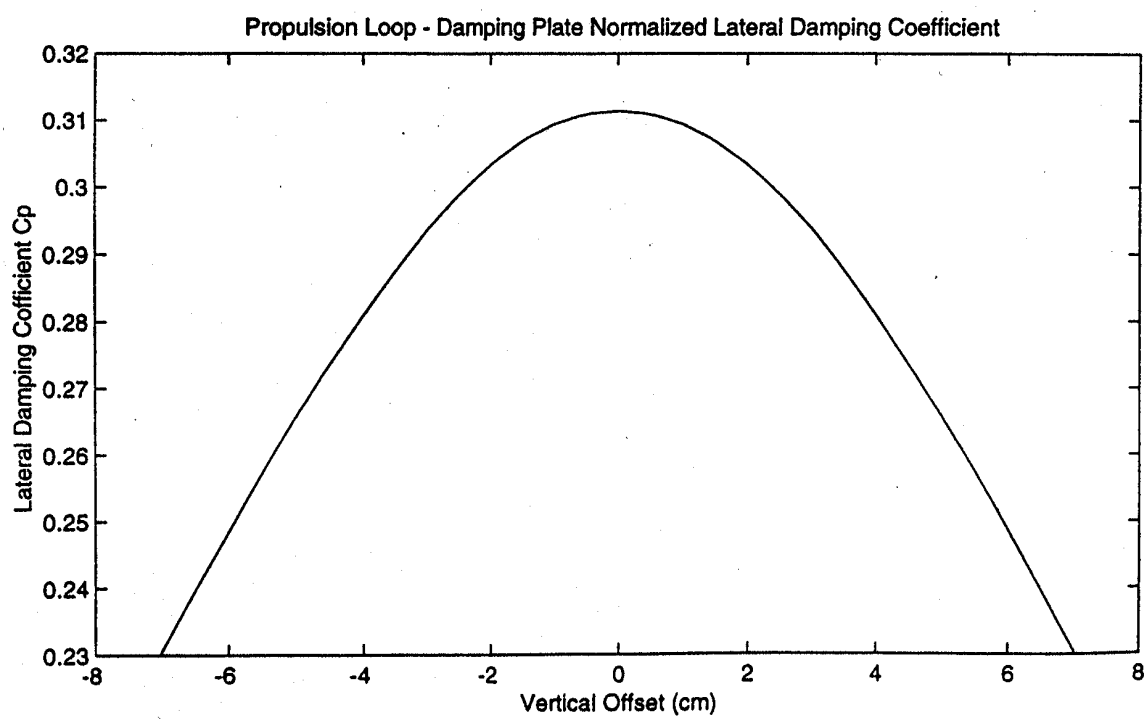

Figure 15. Propulsion Coil – Damping Coil Normalized Lateral Damping Coefficient

6. Summary of Analysis of Passive Damping Mechanisms

In order to compare the various passive damping mechanisms and to help put the results of the above estimates into perspective, it is necessary to relate the various measures of damping commonly used. These include the damping coefficient, the damping factor, the damping force, and the decay time. The damping coefficient (C) was used extensively in Sec's 4 and 5. It has the same physical meaning as the damping coefficient that generally appears in the simple differential equation of motion for a mechanical system:

$$\frac{d^2}{dt^2}x + \frac{C}{M}\frac{d}{dt}x + \frac{K}{M}x = 0\,, \tag{44}$$

where K is a spring constant. It is easily shown that the solution of this differential equation has the form

$$x = e^{-\alpha t}\sin\omega t \tag{45}$$

where α is the damping factor, which has the units of reciprocal time (1/s) and is given by

$$\alpha = C/2M\,, \tag{46a}$$

and the corresponding decay time is given by

$$\tau = \alpha^{-1} \tag{46b}$$

The angular frequency is given by

$$\omega = \sqrt{\frac{K}{M} - \frac{C^2}{4M^2}} \tag{47}$$

Eqn. (44) can also be used to identify the relationship between the damping coefficient and the damping force. Multiplying through by the mass M, the second term in Eqn. (44) becomes the instantaneous damping force. The average damping force may be expressed in terms of an average velocity as follows:

$$\langle F_d \rangle = C v_{avg} \tag{48a}$$

so that

$$C = \langle F_d \rangle / v_{avg} \tag{48b}$$

For simple harmonic motion,

$$v_{avg} = 2\omega A / \pi \tag{49}$$

where A is the amplitude of the oscillatory motion.

In Sec's. 4.2 and 5.2 above, the normalized damping coefficients were reported. The use of normalized damping coefficients is convenient because they are independent of the frequency of the motion resulting from the perturbing force. The unnormalized vertical damping coefficients for the two damping mechanisms discussed in Sec's. 4.2 and 5.2 are shown in Figs. 16 and 17 as functions of the vertical frequency of vibration for three values of the vertical offset. Note that in Fig. 17, the curve for the vertical offset of zero is coincident with the x-axis. The unnormalized lateral damping coefficients are shown in Figs. 18 and 19 as functions of the lateral frequency of vibration for the same three values of the vertical offset.

Eqn. (46) can now be used to relate the magnitudes of these unnormalized damping coefficients to the corresponding decay times. To proceed, it is necessary to determine the portion of the vehicle mass that can be allocated to each SCM. In the case of the Japanese system at Yamanashi, there are eight SCM's per bogie and one bogie per car. Hence, the appropriate value to use for the mass in Eqn. (46) is $M = M_C/8$, where M_C is the car mass, which is approximately 20 tons or 18144 Kg. Hence, α = 2.204e-4 C, and the corresponding decay time (τ) is 4536/C. As indicated in Fig. 16, the maximum value of C_Z is about 500, at less than 1 Hz, which corresponds to a decay time of 9s, which is quite long. As the vertical oscillation frequency increases, the decay time increases. Lateral decay times are longer still. Hence, the damping mechanisms analyzed in Sec. 4.2 and 5.2 are quite weak and are comparable to the intrinsic magnetic damping estimated in Ref. 7. Using the relationship given in Eqn. (48), the average damping forces associated with these damping coefficients are at most 64 N/SCM for oscillations with an amplitude of 0.01 m. This magnitude of damping force can be compared with the estimated damping force associated with eddy currents induced in the guideway conductors (see Sec. 3.2). The results are summarized in Table 6 on a per SCM basis.

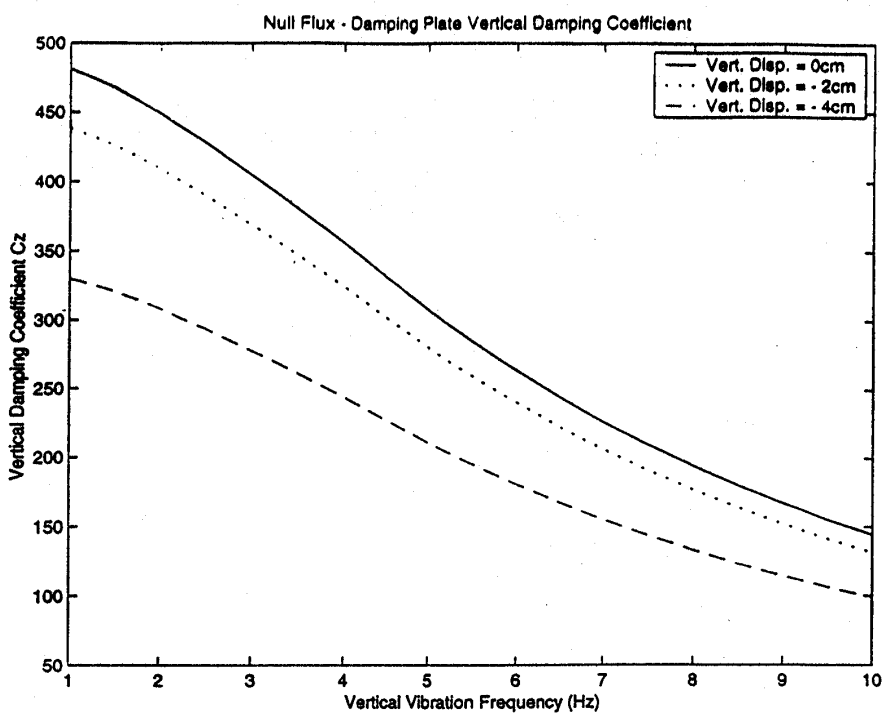

Figure 16. Null-Flux Coil – Damping Loop Vertical Damping Coefficient with Vertical Offset as a Parameter.

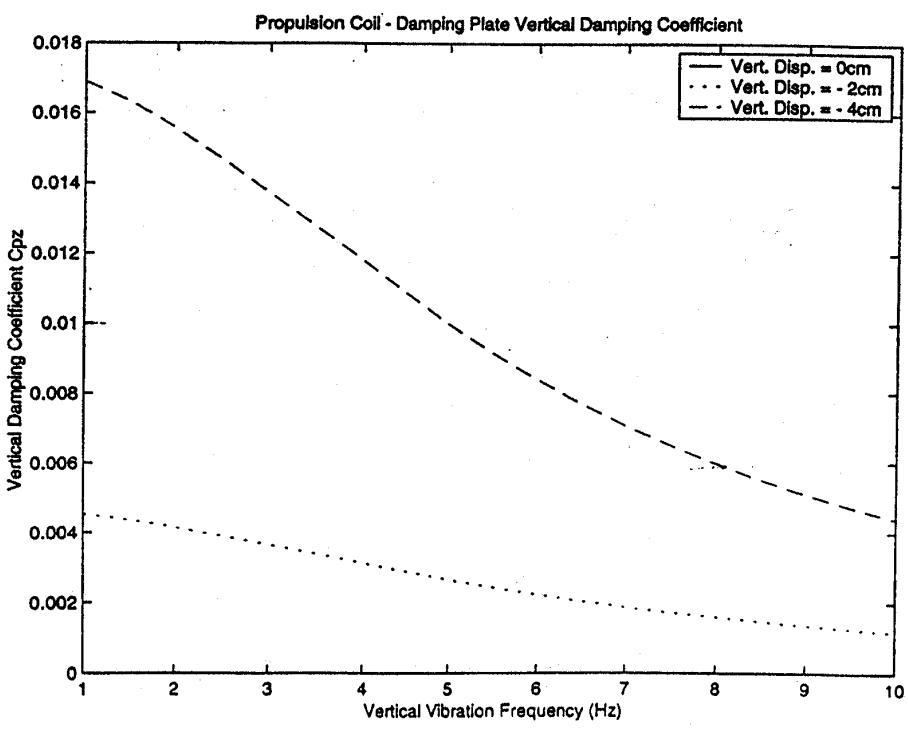

Figure 17. Propulsion Coil– Damping Loop Vertical Damping Coefficient with Vertical Offset as a Parameter.

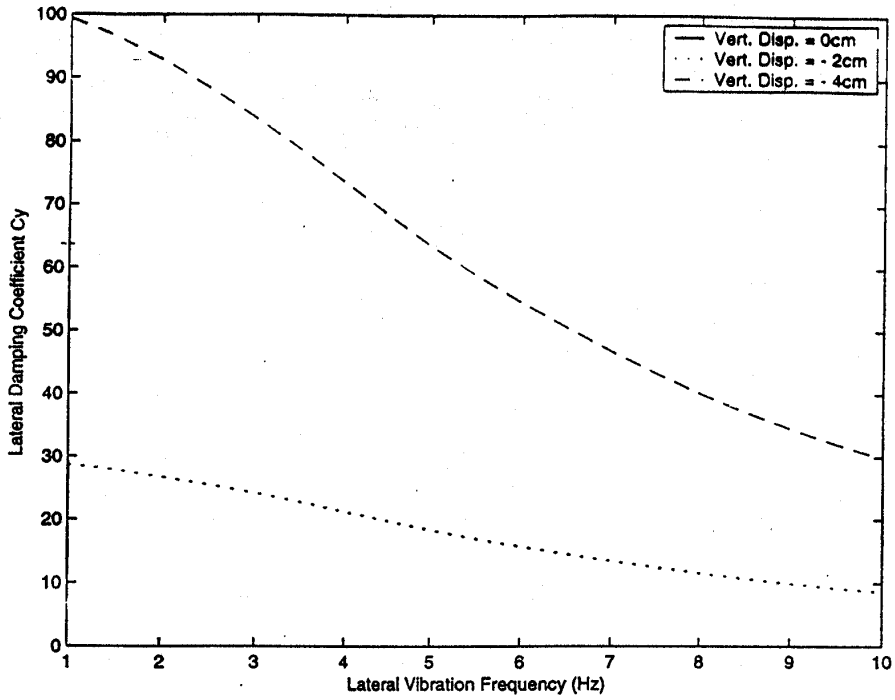

Figure 18. Null-Flux Coil – Damping Loop Lateral Damping Coefficient with Vertical Offset as a Parameter.

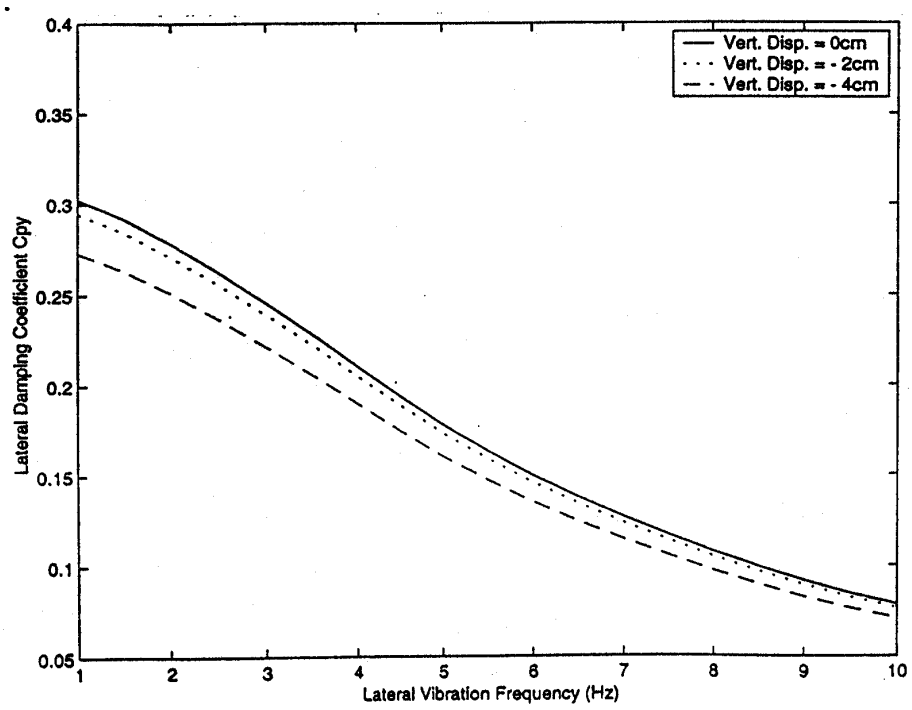

Figure 19. Propulsion Coil – Damping Loop Lateral Damping Coefficient with Vertical Offset as a Parameter.

Table 6 Comparison of Damping Forces per SCM (N/SCM) For Oscillation Amplitude of 0.01 m.

Oscillation Frequency (Hz)	**1**	**2**	**5**	**10**
Eddy Current Vertical Damping in Rebar				
Rebar Radius = 0.00794	0.004	0.008	0.19	0.38
Rebar Radius = 0.0.01588	0.16	0.32	0.80	1.6
Eddy Current Vertical Damping in Null-Flux Coil Conductors				
Conductor Radius = 0.00423	5.7	11.4	28.2	56.5
Conductor Radius = 0.00733	17.0	34.0	84.8	170
Conductor Radius = 0.00156	0.73	1.4	3.7	7.3
Eddy Current Lateral Damping in Null-Flux Coil Conductors				
Conductor Radius = 0.00423	10.2	20.4	50.9	102
Conductor Radius = 0.00733	30.6	61.2	153.0	306
Conductor Radius = 0.00156	1.3	2.6	6.6	13
Induced Current in Damping Plates Simulated by Shorted, Single -Turn Coils Due to				
Vertical Motion Relative to Null Flux Lift Coils				
Z_0 = 0 m	19	36	62	58
Z_0 = 0.04 m	13	25	42	40
Lateral Motion Relative to Null Flux Lift Coils				
Z_0 = 0 m	0	0	0	0
Z_0 = 0.04 m	4.0	7.4	13	12
Vertical Motion Relative to Propulsion Coils				
Z_0 = 0 m	0	0	0	0
Z_0 = 0.04 m	0.0007	0.0012	0.002	0.0005
Lateral Motion Relative to Propulsion Coils				
Z_0 = 0 m	0.012	0.022	0.036	0.024
Z_0 = 0.04 m	0.011	0.020	0.032	0.016

In is interesting to note that in the case of the eddy currents induced in the guideway conductors, the dissipated power goes as the frequency squared and consequently the corresponding damping force goes as the frequency. In contrast, in the case of the currents induced in the vehicle-borne damping coils, the dependence on the oscillation frequency is more complicated. As Eqns. (48) and (49) indicate, the damping force is proportional to v_{avg} ,which, in turn, goes as the frequency. However, the damping coefficient goes inversely as the frequency squared [see Fig. 4 and Eqn. (42)]. Consequently, the damping force first increases then decreases with the frequency.

In the oscillation frequency range of interest, namely 1 to 10 Hz, Table 6 shows that the dominant vertical damping mechanism is the eddy currents induced in the large-radius null-flux coil conductors. However, if these coils are designed to minimize the drag force on the vehicle by minimizing the conductor radius, then the currents induced in the simulated vehicle-borne damping plates become the dominant mechanism.

Similarly, motion in the lateral direction receives the greatest damping due to the eddy currents induced in the large-radius null-flux coil conductors. However, if the small-radius conductors are used in the null-flux coils, then none of the mechanisms examined above produce very much lateral damping. Motion relative to the propulsion coils produces the least amount of damping of any of the damping mechanisms considered here.

Sensitivity of the Damping Force to the Equivalent Coil Resistance

The results obtained in Sec. 4.2 and 5.2 are based on the use of single, shorted -turn coils to simulate the damping effect of plates (the vertical outer cryostat wall facing the guideway). This approach enables the dynamics of the coil system to be taken into account but raises the question of how to define the parameters of the equivalent damping coil. The dimensions of the damping coils were arbitrarily selected so that the thickness equaled that of the plate being simulated, and the length and height equaled that of the coil that produced the field (null-flux loop or propulsion coil). Since this choice of dimensions for the damping coil utilizes only a fraction of the metal in the plate being simulated, the damping coil will have a substantially greater resistance than the plate to currents circulating in it. Hence, the eddy current losses and the damping force could be substantially different.

Calculations of the fields and their derivatives described previously suggests that the currents induced in a flat plate would flow throughout the plate, but be peaked in a path with dimensions similar to those of the coil producing the field. Consequently, while the average current path length in the plate may be similar to that of the damping coil selected above , the cross-sectional area may be much larger. In fact, Saitoh, et al, Ref. 6, who treated the eddy current losses in all three vessel walls using a 2-dimensional finite element approach, showed the greatest damping occurred in the outer vessel wall. In addition, they showed that the induced currents also flowed in the top and bottom of the cryostat walls.

Hence, it seems appropriate to examine the effect of using more metal in the equivalent damping coils on the damping force. In order to make the coil resistance the same as that of the plate would require making the coil cross section much larger which would, in turn, change all the inductance calculations. A more expeditious approach would be to leave the coil dimensions unchanged but adjust the conductivity of the damping coil so its resistance equals that of the average current path in the plate.

This approach reduces the coil resistance but leaves the coil self inductance unchanged, which, in turn, reduces the coil's critical frequency [see Eqns, (27) & (39)].

Table 7 shows the dimensions of the damping plates and coils used to simulate them in the damping force calculations. The upper (or lower) half of the outer vessel wall facing the upper (or lower) null-flux loops plus a portion of the top (or bottom) of the outer vessel constitutes the damping "plate" that is being simulated by a damping coil of the dimensions shown. Similarly, the outer vessel wall facing the propulsion coils plus a portion of the top and bottom of the vessel constitutes the damping "plate" that is being simulated by a damping coil. Expressions for these resistances are given below:

for the damping plates,

$$R_p = \frac{4(\ell_c L_p + h_c H_p)}{\sigma_p T_p H_p L_p}, \tag{50}$$

and, for the damping coils,

$$R_c = \frac{2(\ell_c + h_c)}{\sigma_c h_{cw} t_c}, \tag{51}$$

where L_p, H_p, and T_p are the length, height, and thickness of the damping plate, and l_c,h_c,t_c, and h_{cw} are the length, height, thickness, and width in the coil plane of the damping coil.

As shown in the Table 7, the resistance is much smaller for the plates than for the corresponding damping coils. The resistances of the plates and their corresponding damping coils can be made artificially equal by replacing the conductivity of the damping coil with an effective conductivity given by

$$\sigma_{eff} = \sigma_p \frac{T_p H_p L_p (\ell_c + h_c)}{2 h_{cw} t_c (\ell_c L_p + h_c H_p)} \tag{52}$$

The values of the plate conductivity and the effective damping coil conductivity are also given in Table 7.

An examination of the equations used in the previous sections to estimate the damping coefficients [Eqns. (30), (31), (42), & (43)] shows that the resistance of the damping coil enters the equations in the denominators and in the normalization factors via the critical frequencies. Hence, the dependence of the damping coefficients on the damping coil resistances and the frequency can be expressed as

$$C \propto Q(R_c, f) \quad , \tag{53}$$

where the function Q is given by

$$Q(R_c, f) = \frac{1}{R_c\left[1 + \left(f/f_c\right)^2\right]} . \tag{54}$$

The function Q is plotted as a function of the frequency f in Fig. 20 for two values of the resistance R_c for the null-flux-loop-facing damping coil. The larger and smaller values of R_c correspond to the value used in the previous calculations summarized in Table 6 and the value obtained from using of effective conductivity, respectively. Fig. 21 shows the same plots for the propulsion-coil-facing damping coil. As is clearly shown, the effect of increasing the conductivity of the damping coils in the manner described above is to increase the damping coefficients at low frequency and to make them decrease faster with increasing frequency.

Table 7 Effective Conductivity of Damping Coils

	Null-Flux Damping Plate	Null-Flux Damping Coil	Propulsion Coil Damping Plate	Propulsion Coil Damping Coil
Length	1.35	1.2765	1.35	1.2765
Effective Height	0.545	0.34	1.09	0.60
Thickness	0.015	0.015	0.015	0.015
Resistance of Mean Current Path	0.01962	0.0773	0.0122	0.0897
Conductivity	3.53e7	3.53e7	3.53e7	3.53e7
Effective Conductivity		13.91e7	--	25.95e7
Critical Frequency (from Table 5)		6.44	--	5.81
Critical Frequency (using Effective Conductivity)		1.63	--	0.79

The results of using the effective conductivity in the damping force calculations are summarized in Table 8 using the same format as in Table 6. Comparison of the results in the two tables shows that, except for the shift to lower frequencies, the damping force caused by the damping coil motion relative

to the null-flux coils is not substantially different. The damping effect of the propulsion coils remains relatively insignificant. The decay times associated with these damping forces are inversely proportional to the damping coefficients as shown in Eqn. (46). In the frequency range of 1 to 10 Hz, those times remain of the order of 9s or more.

Based upon the limited sensitivity analysis described above, in the frequency range of 1 to 10 Hz, the method used to select the damping coil properties does not affect the relative importance of the damping associated with eddy currents due to the null-flux and propulsion coils. The frequency at which the peak damping force occurs does depend on the damping coil parameters, but the value of the peak does not.

Table 8 Summary of Damping Forces per SCM (N/SCM) Using the Effective Conductivity for the Damping Coils. Oscillation Amplitude = 0.01 m. Z_0 = Vertical Offset.

Oscillation Frequency (Hz)	**1**	**2**	**5**	**10**
Vertical Motion Relative to Null Flux Lift Coils				
Z_0 = 0 m	56	62	38	20
Z_0 = 0.04 m	39	42	26	14
Lateral Motion Relative to Null Flux Lift Coils				
Z_0 = 0 m	0	0	0	0
Z_0 = 0.04 m	12	13	8	4
Vertical Motion Relative to Propulsion Coils				
Z_0 = 0 m	0	0	0	0
Z_0 = 0.04 m	0.002	0.003	0.0006	0.00009
Lateral Motion Relative to Propulsion Coils				
Z_0 = 0 m	0.035	0.046	0.011	0.004
Z_0 = 0.04 m	0.031	0.041	0.010	0.003

Figure 20. Damping Coefficient Proportionality Constant vs. Frequency for Two Values of Null-Flux Loop Damping Coil Resistance

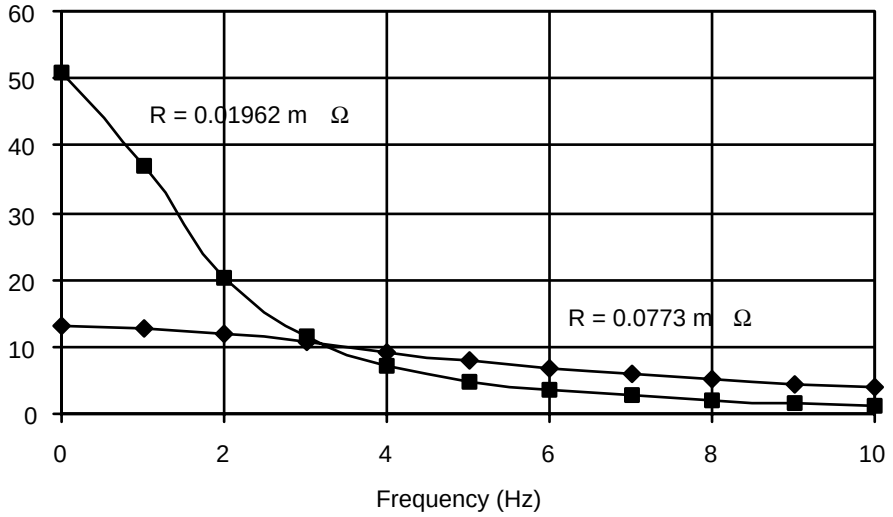

Figure 21. Damping Coefficient Proportionality Constant vs. Frequency for Two Values of Propulsion Coil Damping Coil Resistance

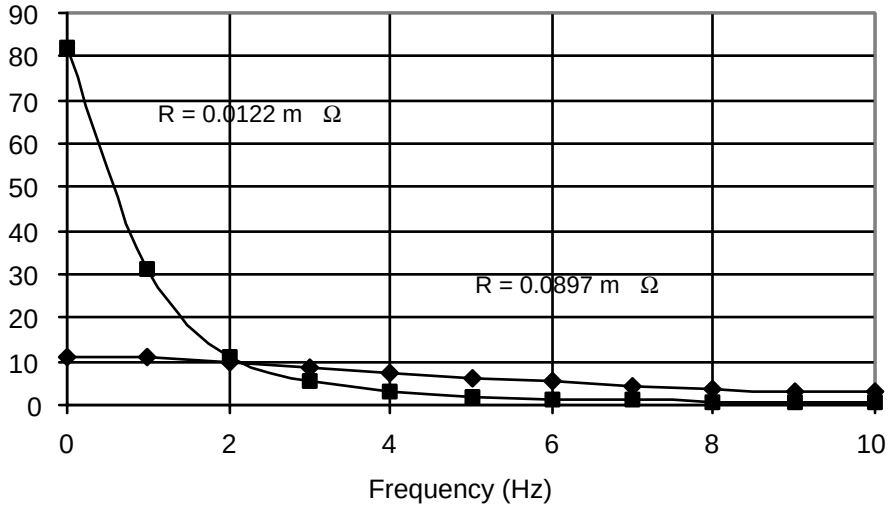

7. Damping Associated With Power Pickup

Electromagnetic induction employing linear generators is a common means of non-contact power transfer from the guideway to the vehicle. Two types of linear generators being developed for use on the Yamanashi test vehicles are described in Ref. 38. (These vehicles require about 50 kW of power each.) One design uses the same SCM's that are used for levitation and propulsion, while the other uses a separate set of dedicated SCM's. Both methods use thin pickup coils mounted on the faces of the SCM's to maximize the coupling with the harmonic fields produced by the guideway-mounted coils. Under steady-state conditions, the fundamental traveling magnetic wave generated by the multiphase excitation of the propulsion windings is at rest relative to the pickup coils and does not induce currents in them. However, the harmonics of the fundamental wave move with respect to the pickup coils and induce current in them. But, the main source of induced current in the generator coils is the harmonic magnetic fields generated by the lift coils interacting with the SCM's.

Assuming an overall efficiency of say 90%, the steady state drag force associated with the operation of the linear generator is expected to be about 360 N per bogie at 156 m/s.

If the vehicle undergoes perturbed motion in response to some disturbance, then that motion will also contribute to the induced current in the pickup coils. To the extent that the energy associated with that component of the induced current is absorbed by the vehicle's electrical load, passive damping of the perturbed motion will result. Consistent with the earlier discussion, the power dissipated by this damping may be of the order of a few percent of the primary vehicle electrical load, say 150 W or so per bogie.

In light of the weak damping associated with the mechanisms described above, several groups have considered using some form of active magnetic damping. Coffey, et al[10] were probably the first to successfully use cryogenically-cooled, actively-controlled damper coils in a large-scale test of an EDS system. Much more recently Ohashi, et al[39] proposed using actively controlled damper coils placed between the SCM's and the lift coils. It has been noted by an RTRI group[9], that while providing adequate damping forces, this approach is not well suited to the Yamanashi test vehicles because of space limitations and the need for exclusive coils, a power source and control equipment on board.

Taking the connection between power pickup and damping one step further, the group at RTRI[9] is investigating the active control of the linear generator system to actively control vehicle damping. In principal, this could be accomplished because the output energy from the linear generator is used to service the vehicle power load and also to recharge onboard batteries used as a power source at low

speed. However, the approach being investigated by the RTRI group is rather different. Their analysis has shown that it is possible, through a clever connection of the pickup coils, to use the on-board power converter to separately control the components of the current induced in the linear generator coil array by the longitudinal and the vertical vehicle motions. Consequently, they state that this control system can maintain the output to the vehicle load and simultaneously control the vertical damping force. They also state that this system will produce damping forces about 70 % those of an active damper coil system without the added problems mentioned above.

8. Conclusions

The preponderance of evidence, both theoretical and experimental, now strongly supports the notion that repulsive-force magnetically levitated systems are naturally under damped and under carefully-controlled laboratory conditions can even exhibit intrinsic negative magnetic damping characteristics. This suggests that, in the absence of any active or enhance passive damping, one or more instabilities may arise in some speed ranges. This appears to contradict the lack of any observation of an instability occurring in tests of large-scale systems. [The one exception to the latter statement is the disclosure in 1998 by RTRI researchers [5] that their repulsive force maglev system shows an instability at low speed that places a lower limit on the liftoff speed. More will be said about this instability later.]

One of the major objectives of this investigation has been to reconcile the lack of intrinsic magnetic damping with the absence of observed dynamic instabilities in large-scale systems. The focus has been on passive damping mechanisms, and whether there are, in fact, sources of enhanced passive damping that can compensate for the lack of intrinsic magnetic damping in repulsive force systems

Estimates were made of the drag force caused by eddy currents induced in guideway electrical conductors, (i.e. non-magnetic rebar, null-flux lift coil conductors, and propulsion coil conductors) during steady-state vehicle motion in the x-direction. The damping force associated with eddy-currents induced in these conductors by unsteady motion (i.e. oscillations in the y or z-directions) were also evaluated.

It was found that the drag forces and damping associated with the eddy currents induced in the guideway conductors increased rapidly with conductor radius. In fact the eddy currents induced in the large-radius null-flux coil conductors by motion in the lateral or vertical directions relative to the superconducting magnets was the dominant source of damping. It was also found that by replacing thick coil conductors with stranded cables using individually insulated strands could substantially reduce the drag force. Unfortunately, the use of such cables also substantially reduced the damping force.

The study also examined damping involving the dissipation of eddy currents induced in vehicle-borne, simulated damping plates by vertical and lateral motions relative to the null-flux lift and propulsion coils fixed to the guideway. Dynamic circuit theory was used to model the interactions between the SCM's, the guideway coils, and the damping plates, which were simulated by single, shorted-turn coils. Two damping coils were used to simulate a damping plate in the case of the null-flux coil induced currents. One damping coil was used in the case of the propulsion coils. The lift currents in the null-flux coils are themselves induced by the longitudinal motion relative to the SCM's on board the vehicle, while the currents in the propulsion coils are the net effect of the induced emf and the voltage applied by an external power supply.

It was found that the damping coefficients decreased with vibration frequency and those ascribed to the null-flux/damping coil interaction were generally much larger than those associated with the propulsion coil/damping coil interaction. The damping forces first increased then decreased with frequency, reaching peak values in the range of 1 to 10 Hz. At the null-flux or neutral position, the null-flux-based mechanism produced no lateral damping while the propulsion-coil mechanism did produce some damping, although it was not significant. It is important to point out that with sheet guideways or those using conventional as opposed to null-flux lift coils, there would be no null-flux position at which the lateral damping goes to zero.

When the null-flux coils were designed to minimize the steady-state drag force, the eddy currents induced in the vehicle-borne, simulated damping plates by the null-flux coils became the dominant source of damping in the vertical direction. This mechanism also yielded the largest lateral damping except near the null-flux position, where it went to zero. The damping in the vertical direction decreased with the displacement from the null-flux position while the lateral damping increased. However, even the maximum vertical damping by this mechanism was relatively small, corresponding to a decay time of about 9s. While this degree of vertical damping is sufficient to overcome the intrinsic negative damping described in the introduction, it is still relatively weak for ride comfort purposes. Typically, one would like to see a decay time closer to 1 or 2s.

The absence of significant lateral damping by any of the mechanisms examined (when small-radius conductors were used in the guideway) was an important finding for the null-flux lift coil-based maglev system. On the one hand, it suggests that some form of active damping is definitely required. On the other, it helps to explain the need to have a relatively high lift-off speed in the Japanese maglev system and also the instability observed by the RTRI researchers [5] near lift off. Below the lift-off speed the lift and guidance forces are relatively weak and the vehicle must be mechanically supported near the null-flux position to minimize the drag force. Under those conditions, based on the results obtained here, the lateral damping is very small, especially if the rebar and coil conductors are

designed to minimize the drag force. Hence, any disturbance in the lateral direction would tend to be under damped. However, in the case of the reported instability, it is due not only to the lack of lateral damping but also to the geometry of the magnet/guideway coil configuration, which is consistent with a sway-roll static instability as discussed in the main text.. The relative loss of damping when the large diameter null-flux conductors are replaced by small diameter, individually insulated ones suggests that early tests at Miyazaki may have shown greater damping from this mechanism than subsequent tests at Yamanashi, where coils designed to reduce the drag-force were presumably used.

The calculation of the damping coefficients for the null-flux/damping plate and the propulsion coil/damping plate interactions was based on a dynamic circuit theory model. This model uses an equivalent coil to simulate the damping action of the damping plate in both cases. While this model allows one to include the interactions of several neighboring coils, it suffers from the weakness that the choice of equivalent coil parameters is somewhat arbitrary. A brief sensitivity study showed that the magnitude of the peak damping force in the range of 1 to 10 Hz was not very sensitive to the choice of coil parameters, but that the frequency dependence was. By increasing the conductivity of the equivalent coil to simulate the use of a larger coil cross-sectional area, the damping force peak was shifted to a lower frequency. Time did not permit a more detailed exploration of damping coil parameter changes such as using a large cross-section coil with increased conductivity. Such a coil design would likely result in increased passive damping, but would not alter the relative contributions of the null-flux and propulsion coils, nor would it change the absence of damping at the null-flux position.

It should be pointed out that for the calculations performed here, only the damping effect of the outer cryostat walls were taken into account. Inclusion of the middle and inner vessel walls would have increased the damping in both the vertical and lateral directions somewhat. The greatest penetration of the outer vessel wall would be expected at the lowest frequencies (a few Hz). One can therefore speculate with some confidence that this greater penetration to the radiation shield and the inner vessel walls would lead to enhanced damping and help to account for the stability seen in the earlier tests at the Miyazaki test track. (Of course, the greater degree of penetration would also lead to greater heat input to the liquid helium coolant.) Certainly, other forms of enhanced passive damping, including aerodynamic and mechanical mechanisms (not treated in this report) undoubtedly also contributed to the overall system damping at moderate to high speeds. A final point in this regard, is that when the early tests were conducted at Miyazaki, the guideway used only conventional in lieu of null-flux coils.

One way to significantly enhance the passive damping mechanisms described above would be to significantly reduce the vehicle-borne damping coil resistance while at the same time reducing its self-inductance. This could be accomplished by increasing the cross-sectional area of the coil and increasing the conductivity. The latter could be accomplished by reducing the coil temperature to near or below that of liquid nitrogen. In principle, such modifications could reduce the damping coil

resistance by an order of magnitude or more, without decreasing the critical frequency as much as occurred in the sensitivity study mentioned above. The result would have been a significant increase in damping force and a corresponding decrease in the decay time to perhaps one to three seconds. Decay times in that range would approach critical damping and would be highly desirable for a passenger vehicle. In this connection, it is worth noting that in the case of the tests performed at SRI in the early seventies, passive damping coils were placed inside the cryostats and cooled to liquid nitrogen temperatures. Those damping coils had large cross-sectional areas and could have provided enough passive damping to suppress any instabilities in the speed range tested.

The net effect of all of the passive damping mechanisms examined here appears to be sufficient to overcome the intrinsic negative damping seen in some laboratory experiments and to contribute some net positive damping particularly of large amplitude oscillations in the vertical direction. If large diameter rebar and null-flux conductors were used at Miyazaki test track, that together with the use of conventional lift coils could explain the lack of any observations of instabilities there. When the rebar and null-flux lift coils are designed to minimize the steady-state drag forces, the net passive damping is considerably reduced. In particular, in the lateral direction the net damping was found to be very small, suggesting an under damped condition especially near lift off. The use of enhanced passive damping similar to that used by SRI in the early seventies or active damping using the linear generator appears to be possible solutions. Although there are alternative repulsive force suspension system design under various stages of development, they could not be investigated within the scope of this study.

References

1. Cai, Y. and D. M. Rote, A Review of Dynamic Stability of Repulsive Force Maglev Suspension Systems, Proceedings of the Maglev'98 Conference held in Yamanashi, Japan in April, 1998, published by IEEJ, pg. 231-236, 1998.

2. Cai, Y., D. M. Rote, T. M. Mulcahy, Z. Wang, S.S. Chen, and S. Zhu, Dynamic Stability of Repulsive-Force Maglev Suspension Systems, Argonne National Laboratory Report No. ANL-96/18,Nov. 1996.

3. He, Jianliang, and C. Coffey, Magnetic Damping Forces in Fig.-Eight-Shaped Null-Flux Coil Suspension Systems, presented at the INTERMAG 97 Conference, April 1, 1997.

4. Higashi, K., S. Ohashi, H. Ohsaki, and E. Masada, Mechanism of Magnetic Damping in the Superconducting Magnetic Levitation System, Proceedings of The First International Symposium on Linear Drives for Industry Applications, LIDA'95, held in Nagasaki, Japan, published by IEEJ, pg. 131-134,1995.

5. Yoshioka, H., E. Suzuki, H. Seino, M. Azakami, H. Oshima, and T. Nakanishi, Results of Running Tests and Characteristics of the Dynamics of the MLX01 Yamanashi Maglev Test Line Vehicles, Proceedings of the Maglev'98 Conference held in Yamanashi, Japan, published by IEEJ, pg. 225-230, April,1998.

6. Saitoh, T., N. Maki, T. Kobayashi, M. Shibata, and T. Takizawa, Electromagnetic Force and Eddy Current Loss in Dynamic Behavior of a Superconducting Magnetically Levitated Vehicle, to be published.

7. He, J. L., D. M. Rote, and S. S. Chen, Characteristics and Computer Simulation of Magnetic Damping Forces in Maglev Systems, Argonne National Laboratory Report No. ANL/ESD/TM-66, May 1994.

8. Cai, Y., S. S, Chen, T. M. Mulcahy, and D. M. Rote, Dynamic Stability of Maglev Systems, Argonne National Laboratory Report No. ANL-92/21, April, 1992.

9. Murai, T., H. Hasegawa, T. Yamamoto, and S. Fujiwara, Active Magnetic Damper Using Linear Generator of EDS Maglev, Proc. Of the Maglev'2000 Conference held in Rio de Janeiro, pp. 191-196, June, 2000.

10. Davis, L. C. and D. F. Wilkie, Analysis of Motion of Magnetic Levitation Systems: Implications for High Speed Vehicles, Journal of Applied Physics, Vol. 42, No. 12, pp 4779-4793, Nov. 1971.

11. Iwamoto, M., T. Yamada, and E. Ohno, Magnetic Damping Force in Electrodynamically Suspended Trains, IEEE Trans. on Mag., Vol. Mag-10, No. 3, pp 458-461, Sept. 1974.

12. Fujiwara, S., Damping Characteristics of the Repulsive Magnetic Levitation Vehicle, Japanese Railway Technical Research Institute, Quarterly Reports, Vol. 21, No. 1, pp 49-52, 1980.

13. Fujiwara, S. and H. Takashi, Damping Characteristics and AC Magnetic Field of Repulsive Magnetic Levitation, Japanese Railway Technical Research Institute, Quarterly Reports, Vol. 24, No. 2, pg 93, 1983.

14. Moon, F.C., Vibration Problems in Magnetic Levitation and Propulsion, Chapter 6 in Transport Without Wheels, Ed. E. R. Laithwaite, Elek Science, London, pp122-161, 1977.

15. Zhu, S., Y. Cai, D. M. Rote, and S. S. Chen, Magnetic Damping For Maglev, Shock and Vibration, Vol. 5, No. 2, pp 119-128, 1998.

16. Coffey, H. T., et al, Dynamic Performance of the SRI Maglev Vehicle, IEEE Trans. Mag., 3, pp. 451-457, 1974 Also see references therein to earlier reports by Coffey, et al.

17. Sato, Y., Matsuura, A., Miura, S., and Satoh, Y., Development of Guideway for Maglev, Proc. Int. Conf. On Maglev Transport "85, Tokyo, Sept. 17-19, pp. 243-250, 1985.

18. Tanaka, H., Operational Experience of JNR'S Maglev Test Train, Proc. Int. Conf. On Maglev Transport "85, Tokyo, Sept. 17-19, pp. 271-276, 1985.

19. Yoshioka, H. and M. Miyamoto, Dynamic Characteristics of Maglev Vehicle MLU001-Guideway Irregularity Test-, Proceedings of the International Conference on Maglev & Linear Drives, Vancouver, B. C., Canada, May 14-16, pp 89-94, 1986.

20. Moon, F. C., Nonconservative Instabilities in Electrodynamic Magnetic Levitation of Vehicles, Proceedings of the International Seminar on Superconductive Magnetic Levitated Train, Miyazaki, Japan, Nov. 9-10, pp108-112, 1978.

21. Chu, D., and F. C. Moon, Observations of Dynamic Instabilities in Magnetically Levitated Models, Proceedings of the International Seminar on Superconductive Magnetic Levitated Train, Miyazaki, Japan, Nov. 4-5, pp 136-141,1982.

22. Kolm, H., Why Magneplane is the only Stable EDS, Memorandum from H. Kolm, Magneplane International Inc., Jet Aviation Terminal, Hanscom Field, Bedford, MA. to John Harding, National Maglev Office, Federal Railroad Administration, Washington, DC, July 7, 1993.

23. He, J. L., D. M. Rote, Z. Wang, and H. T. Coffey, Dual-Keel Electrodynamic Maglev System, Proceedings of the Maglev'95 Conference, p. 153-158, November, 1995.

24. Davey, K., T. Morris, D. Rote, and R. Zowarka, An Integrated Maglev System, Proceedings of the Maglev'98 Conference, p. 297-305, April, 1998.

25. Coffey, H. T., J. D. Colton, and K. D. Mahrer, Study of a Magnetically Levitated Vehicle, Final Report Task II, prepared for the Federal Railroad Administration, Report No. FRA-RT-73-24, Feb. 1973.

26. Jizo, Y., Y. Furuta, H. Nakashima, and T. Iwahana, Superconducting Magnet for Maglev Train, Proc. Int. Conf. On Maglev Transport "85, Tokyo, Sept. 17-19, pp. 185-192, 1985.

27. He, J. L., D. M. Rote, and H. T. Coffey, Study of the Japanese Electrodynamic Suspension Maglev Systems, Argonne National Laboratory Report No. ANL/ESD-20, April, 1994.

28. Fink, D. G., and H. W. Beaty, Standard Handbook for Electrical Engineers, 12th Edition, McGraw-Hill Book Co. N.Y., 1987.

29. Zahn, M. Power Dissipation and Magnetic Forces on Maglev Rebar, Massachusetts Institute of Technology, Dept. of Electrical Engr. and Computer Science, prepared as a supplement to "Investigation of the Deleterious Effects of Electro-Magnetic Fields on Steel Rebar Used in Guideways for EDS Maglev Systems", Final Report, Volume 1, Summary, Oct 13, 1995, by R. D. Thornton, et al, to the Federal Railroad Administration.

30. Thornton, R. D., et al, Investigation of the Deleterious Effects of Electro-Magnetic Fields on Steel Rebar Used in Guideways for EDS Maglev Systems, Final Report to the Federal Railroad Administration, Volume 1, Summary, Oct 13, 1995,

31. Terai, M., S. Inadama, H., Tsuchishima, E., Suzuki, and T. Okai, Development of New Superconducting Magnets for the Yamanashi Line , Proceedings of the Maglev'95 Conference, p. 267-274, November, 1995.

32. Nakashima, H., M. Terai, M. Shibata, M. Yamazi, and Y, Jizo, Superconducting Magnet and Refrigeration System for Maglev Vehicle, Proceedings of the Maglev'93 Conference, p. 160-164, May, 1993.

33. Hidenari, A., Y Takashi, Y. Jizo, M. Terai, M. Shinobu, H. Tsuchishima, Approach to Reducing Heat Load of Superconducting Magnets for Maglev Trains, Proceedings of the Maglev'95 Conference, pp 275-280, November, 1995.

34. Murai, T. and S. Fujiwara, Design of Coil Specifications in EDS Maglev Using an Optimization Program, Proceedings of The Second International Symposium on Linear Drives for Industry Applications, LIDA'98, Tokyo, Japan, pp 343-346, 1998.

35. Tsuchishima, H., T. Mizutami, T. Okai, M. Nakauchi, M. Terai, S. Inadama, T. Asuhara, Characteristics of Superconducting Magnets and Cryogenic System on Yamanashi Line, Proceedings of the Maglev'98 Conference, pp. 237-243, 1998.

36. Nakao, H.,M. Takahashi, Y. Sanada, T. Yamashita, M. Yamaji, A. Miura, M. Terai, M. Igarashi, T. Kurihara, K. Tomioka, Development of the New Type On-Board GM Refrigeration System for the Superconducting Magnet in Maglev Use, Proceedings of the Maglev'98 Conference, pp. 250-255, 1998.

37. He, J. L., T. M. Mulcahey, D. M. Rote, and T. Kelly, Computer Modeling and Experimental Verification of Figure-Eight-Shaped Null-Flux Coil Suspension System, Argonne National Laboratory Report No. ANL/ESD/TM-79, Dec., 1994.

38. Murai, T., S. Fujiwara, H. Hasegawa, K. Nemoto, H. Watanabe, Y. Furukawa, M. Shinobu, M. Igarashi, S. Inadama, H. Akagi, and M. Oki, Development of Linear Generators for Superconducting Maglev, Proceedings of the Maglev'2000 Conference, Rio De Janeiro, pp. 262-267, June, 2000.

39. Ohashi, S., H. Osaki and E. Masada, Improvement of the Damping Characteristics for the Superconducting Magnetically Levitated Transportation System. Trans. SICE, Vol. 12, No. 9, pp. 566-574, Sept. 1999.